Measurement of the charge symmetry breaking d+d→^{4}He+π^{0} reaction near threshold

A. D. Bacher, M. A. Pickar, E. J. Stephenson, C. E. Allgower, C. M. Lavelle, H. Nann, J. Olmsted, P. V. Pancella, and T. Rinckel

Phys. Rev. C **99**, 015502 — Published 28 January 2019

DOI: 10.1103/PhysRevC.99.015502

Observation of the Charge Symmetry Breaking $d + d \rightarrow {}^4He + \pi^0$ Reaction Near Threshold

A.D. Bacher,[1,2] M.A. Pickar,[3] E.J. Stephenson,[1,4] C.E. Allgower,[5] C.M. Lavelle,[1,6] H. Nann,[1,2] J. Olmsted,[1] P.V. Pancella,[7] and T. Rinckel[1,4]

[1] *Indiana University Cyclotron Facility, Bloomington, Indiana 47408 USA*
[2] *Department of Physics, Indiana University, Bloomington, Indiana 47405 USA*
[3] *Department of Physics and Astronomy, Minnesota State University at Mankato, Mankato, Minnesota 56001 USA*
[4] *Center for Exploration of Energy and Matter, Indiana University, Bloomington, Indiana 47408 USA*
[5] *Roudebush VA Medical Center, 1481 West 10th Street, Indianapolis, Indiana 46202 USA*
[6] *The Johns Hopkins University Applied Physics Laboratory, Laurel, Maryland 20723*
[7] *Physics Department, Western Michigan University, Kalamazoo, Michigan 49008 USA*

(Dated: October 25, 2018)

We describe the observation of the isospin violating and charge symmetry breaking reaction $dd \rightarrow \alpha\pi^0$ just above threshold. Measurements using a magnetic channel (gated by two photons) of the ^{4}He scattering angle and momentum (from time of flight) permitted reconstruction of the π^0 "missing mass," the quantity used to separate distributions of $^4\mathrm{He} + \pi^0$ events from a continuum containing $^4\mathrm{He} + \gamma + \gamma$ and $^4\mathrm{He} + \pi^0 + \gamma$ events. A review has been completed of the apparatus, relevant GEANT simulations, various corrections, and the $d + p$ scattering cross section used as a luminosity calibration. The new values of the total cross section for neutral pion production are 14.3 ± 2.2 (stat) ± 1.6 (sys) pb at 228.5 MeV and 17.3 ± 3.4 (stat) ± 2.4 (sys) pb at 231.8 MeV. The uncertainty remains dominated by statistical errors. These cross sections arise from the down-up quark mass difference and quark electromagnetic effects.

PACS numbers: 24.80.+y, 24.85.+p, 25.10.+s, 25.45.-z

I. INTRODUCTION

The invariance of baryon properties when up and down quarks are exchanged is known as charge symmetry. This symmetry is broken for electromagnetic properties by the different charges of the two quarks. A consideration of these electromagnetic effects explains most, but not all, of the binding energy difference between ^{3}H and ^{3}He [1]. A similar conclusion was reached for other mirror pairs of nuclei [2]. It is now clear that the unexplained part of the binding energy differences between mirror nuclei, as well as the neutron-proton mass difference, originates from the unequal masses of the up and down quarks ($m_\mathrm{d} > m_\mathrm{u}$) [3–5] and is called charge symmetry breaking (CSB).

The connection between quark CSB processes and effects at the nuclear level is made explicitly in chiral effective field theory [6, 7]. In leading order, two Lagrangians (see Eqs. (1) and (2) of Ref. [7]) are used to represent the contribution from the quark mass difference

$$\mathcal{L}_{qm}^{(1)} = \frac{\delta m_N}{2}\left(N^\dagger \tau_3 N - \frac{2}{DF_\pi^2} N^\dagger \pi_3 \pi \cdot \tau N\right) \quad (1)$$

and electromagnetic (hard photon) processes

$$\mathcal{L}_{hp}^{(-1)} = \frac{\bar{\delta} m_N}{2}\left(N^\dagger \tau_3 N + \frac{2}{DF_\pi^2} N^\dagger (\pi_3 \pi \cdot \tau - \pi^2 \tau_3) N\right) \quad (2)$$

and whose strengths are δm_N and $\bar{\delta} m_N$ respectively. Fields are represented by N for the nucleon and π for the pion. The parameter F_π is the pion decay constant, $D = 1 + \pi^2/F_\pi^2$, and τ represents the Pauli spin matrices in isospin space. To determine the size for the two strengths, experimental information is needed on some CSB pion-nucleon scattering process (described by the second term in Eqs. (1) and (2)) in addition to the neutron-proton mass difference that is given by the sum of the first terms in Eqs. (1) and (2). At the low energies most suitable to chiral effective field theory analysis, evidence on pion-nucleon scattering is restricted to the elastic scattering and charge exchange reactions induced by charged pions on proton targets ($\pi^+ p \rightarrow \pi^+ p$, $\pi^- p \rightarrow \pi^- p$, and $\pi^- p \rightarrow \pi^0 n$). Extracting the quark-induced CSB effect from these data is complicated by the necessity to make corrections to the measured cross sections for the neutron-proton mass difference and the electromagnetic interactions between the pions and the nucleons [8–10].

The alternative is to observe CSB effects in reactions where a pion is produced at a vertex with one nucleon and rescatters from a second as it is emitted from the reaction on-shell. This operator introduces a different combination of δm_N and $\bar{\delta} m_N$ from the neutron-proton mass difference. The opportunity to effect a separate measurement of these strengths was a motivator for the experiments to measure the fore-aft asymmetry in $np \rightarrow d\pi^0$ [11] and the total cross section in $dd \rightarrow \alpha\pi^0$ [12], both reported in 2003. Initial calculations focused on a transferred π^0 in this model with the CSB Lagrangians appearing at the rescattering vertex. Later improvements, reviewed in [5], included $\pi^0 - \eta$ and $\rho^0 - \omega$ [13] mixing along with Δ production without reaching quantitative agreement with either of the pion-production CSB experiments. More recently, the neutron-proton mass difference has been included at the pion-production vertex

[14], requiring the transfer of a charged pion with charge exchange at the rescattering vertex. This diagram adds a different combination of Lagrangian terms at leading order, making the $np \to d\pi^0$ experiment exclusively sensitive to δm_N and in agreement with estimates of δm_N from the neutron-proton mass difference (using [15] to remove the electromagnetic part) and lattice QCD [16].

For CSB to be easily manifest in a π^0-production reaction, the entrance channel should be self-conjugate under the charge symmetry operation. In $np \to d\pi^0$ [11], charge symmetry reflects the entrance channel along the beam direction, so CSB appears as a fore-aft asymmetry in the cross section, $\sigma(\theta) \neq \sigma(\pi - \theta)$. A non-zero result for this asymmetry has been reported to be $A^{fb} = [17.2 \pm 8(\text{stat}) \pm 5.5(\text{sys})] \times 10^{-4}$. In the case of the $dd \to \alpha\pi^0$ reaction, the deuteron is already self-conjugate under the charge symmetry operation. Likewise, the ^{4}He (α) nucleus is self-conjugate, but the π^0 wave function is not, as it is one member of an isospin triplet state. Thus, any amplitude for this process violates charge symmetry. Alternatively, the $dd \to \alpha\pi^0$ reaction is forbidden because it does not conserve isospin. Charge symmetry is the more restrictive of these two requirements. Values of the total reaction cross sections for $dd \to \alpha\pi^0$ have been previously reported [12] to be 12.7 ± 2.2 pb (at 228.5 MeV) and 15.1 ± 3.1 pb (at 231.8 MeV), energies that are just above threshold.

Calculations [7] initially showed a large contribution to the fore-aft asymmetry in $np \to d\pi^0$ from the CSB effects in π^0 rescattering. Unfortunately, this calculation was later found to be wrong by a factor of 4 [14], thus changing the estimates reviewed in [5] in which meson mixing terms were also included. Introduction of the neutron-proton mass difference at the pion production vertex means that the nucleons must be different between the entrance and exit channels (either neutron or proton), giving rise to a charged pion whose charge depends on the sense of the charge transfer. When these two diagrams are included with the original π^0 production and rescattering, the leading order amplitude depends only on the second term in Eq. (1). This permits an estimate of the strong interaction contribution to CSB from the fore-aft asymmetry alone. At leading order, the strong interaction contribution to the neutron-proton mass difference from $np \to d\pi^0$ is 1.5 ± 0.9 MeV. This compares well with the value taken from the experimental neutron-proton mass difference with a correction from the Cottingham sum rule [15] for the electromagnetic contribution, giving 2.0 ± 0.3 MeV. The estimate from lattice QCD is 2.26 ± 0.72 MeV. A re-examination of meson mixing and higher-order terms in light of this analysis would be desirable.

The contributions from pion rescattering and meson mixing are expected to appear with a different balance in the $dd \to \alpha\pi^0$ reaction. Initial work led to a particular sensitivity to $\pi^0 - \eta$ mixing, and the cross section estimates were a factor of several larger than the experimental values [16–19]. These estimates have not been re-examined in light of [14], and it has become clear that a detailed and accurate description of the initial channel distortions is needed before a realistic estimate becomes possible. Work on the description of the entrance channel is underway [17]. There is also a review article that provides a survey of charge symmetry breaking operators [18].

The first $dd \to \alpha\pi^0$ cross section estimates [19, 20] made use of plane waves in the entrance and exit channels as well as simple Gaussian wave functions for the nuclear bound states. Under these conditions the contribution from pion rescattering is particularly small because of the momentum mismatch and the cancellation of the non-recoil part of the amplitude [18]. This leaves photon exchange along with meson mixing (both $\pi^0 - \eta$ and the better known $\rho^0 - \omega$ [13]) as the dominant contributions. Further improvements to the nuclear wave functions included isospin mixing and enhanced strength at large momenta, thus increasing the predicted $dd \to \alpha\pi^0$ cross section to values significantly above the measurements [21]. In a similar fashion, the inclusion of entrance channel distortions through an approximation to a full four-body treatment [18] leads to a further increase in the predicted cross section. These predictions can be brought to within a factor of three of the measured values by adopting a much smaller value of the $\pi^0 - \eta$ mixing [18] than was used for the estimates reported for $np \to d\pi^0$ [7]. Further work is needed to develop the four-body theory to the point where it can provide a better description of the cross section and analyzing power data for the $d + d$ elastic scattering channel [24]. A rescaling of the $\pi^0 - \eta$ contribution changes the predictions for the $np \to d\pi^0$ fore-aft asymmetry as well. A new set of calculations containing a more complete set of diagrams for this process is underway, beginning with the charge symmetry conserving part of the pion production amplitude [21].

Since the special character of the $dd \to \alpha\pi^0$ reaction as a test of charge symmetry was discussed by Lapidus in 1956 [25], several experimental searches have been conducted without success (see [26] for a review). The most recent prior experiment, conducted at Saclay, reported a cross section of $d\sigma/d\Omega = 0.97 \pm 0.20 \pm 0.15$ pb/sr at $\theta_{c.m.} = 107^\circ$ and $T_{lab} = 1.10$ GeV [27]. However, this experiment did not clearly distinguish the CSB $dd \to \alpha\pi^0$ reaction from the isospin-allowed double radiative capture $dd \to \alpha\gamma\gamma$ reaction. Subsequently, it was pointed out that the size of the reported cross section was comparable to the calculated value for the double radiative capture process [28] based on mechanisms similar to those used in the successful treatment of double pion production [29]. Since these two reactions may have similar cross sections, an α in coincidence with a single γ is insufficient as a marker of the $dd \to \alpha\pi^0$ process; one must make a kinematic reconstruction of the final state that demonstrates that the ^{4}He nucleus was produced in a two-body reaction where the other particle had the mass of the π^0.

Based on this experience, the requirement to be able to make this separation became the most prominent de-

sign goal of our experiment. In addition, based on an estimate [20, 30] of the CSB total cross section of 20 pb at an energy of 231.4 MeV, we endeavored to design an experiment with a sensitivity level of 1 picobarn.

We begin in the next section with an overview of the experimental apparatus. Then in Section III we describe the commissioning of the apparatus using the $pd \to h\pi^0$ ($h \equiv {}^3$He) calibration reaction. In Section IV we describe the methods used to arrive at a proper normalization of our measured yields for $dd \to \alpha\pi^0$, including the $d + d$ elastic luminosity monitor reaction, the $d + p$ elastic reference reaction, and cross calibrations. In Section V we describe the analysis of the primary data, including the separation of the $\alpha\pi^0$ events from the $\alpha\gamma\gamma$ and $\alpha\pi^0\gamma$ events. Finally we will discuss the results and offer some concluding remarks.

II. EXPERIMENTAL APPARATUS

A. Overview

The electron-cooled storage ring (Cooler) at the Indiana University Cyclotron Facility [31] offered a particularly clean environment in which to observe pion production reactions near threshold because of the small size of the beam (typical diameter $\sim$ 2 mm) and the use of windowless gas jet targets.

Just above the threshold energy of 225.5 MeV, all of the recoil ^{4}He nuclei from the $dd \to \alpha\pi^0$ reaction emerge into a narrow cone surrounding the beam. One of the six sides of the Cooler ring contained a 6° bend. If the deuterium gas jet target is placed upstream of this bend, then the cone of recoil ^{4}He nuclei can be bent away, as it has about half of the rigidity of the circulating beam. This opens a window of several MeV above threshold in which the recoil cone can be captured completely with a magnetic septum. Previous experiments in the Cooler, e.g. [32], have successfully used a small aperture magnetic channel to capture and identify recoil reaction products at this location in the Cooler ring.

A crucial design requirement of this experiment was to ensure that the photons from the decay of the π^0 could be detected with good efficiency both to cleanly identify the $\alpha\pi^0$ final state and to remove background events. Because of the low velocity of the reaction products in the center of mass frame near threshold, the two photons from π^0 decay emerge in the lab with large opening angles (typically $> 140°$) and angular distributions that are within a factor of two of being isotropic. Thus we were able to design two arrays of modular Pb-glass detectors that could be mounted on the left and right sides of the beam and that, with a solid angle of about 3 sr each, would offer about a 1:3 chance of capturing both π^0 decay photons.

The layout of the experiment as built is shown in Fig. 1. The gas jet target was located upstream of the 6° bending magnet. The gas exits the gas jet moving upward toward the circulating beam. The advantage of such a target is that there are no walls to create other reactions. At the energies of this experiment we were below threshold for the $(d, \alpha\pi^0)$ reaction on all stable nuclei except deuterium. Still, there were about three orders of magnitude more ^{4}He nuclei identified by the magnetic channel than were subsequently associated with the $dd \to \alpha\pi^0$ reaction. These may have originated from (d,^{4}He) reactions on residual gas and storage ring apertures. This background was eliminated by the coincidence requirement of a high-energy gamma ray in each of the two Pb-glass detector arrays.

The side walls of the target box were thin to allow photons to pass with minimal interaction. On the left and right sides of the target box were two arrays containing a total of 250 Pb-glass detectors. The arrangement shown in Fig. 1 is a horizontal section through this array located at the height of the beam. The Pb-glass detectors were relatively insensitive to the large fluxes of charged particles and neutrons from the target region.

In the 6° bending magnet the circulating deuteron beam was bent by 6° while the recoil ^{4}He nuclei were bent by about 12.5°. As shown in Fig. 1, this allowed a further separation to be imposed downstream. On the right side is a small tube which surrounded the deuteron beam on its way to the next quadrupole (shown in Fig. 1) in the Cooler ring. On the left, another channel led to a strong-field septum magnet which bent the recoil nuclei by about another 24° so that there would be room for additional focusing elements along this line.

The detectors in the channel were required to accomplish three tasks. First, recoil ^{4}He (or ^{3}He) events were identified by their energy loss in a series of three plastic scintillators (ΔE1, ΔE2, and E in Fig. 1). Second, the z-component of the recoil momentum was measured using time of flight between the first scintillator (ΔE1) located between the septum magnet and the quadrupole triplet and the scintillator pair at the end of the channel (ΔE2 and E) some 6 m downstream. Third, the transverse momentum component of each recoil was calculated from a measurement of its scattering angle in a wire chamber (WC1) located in front of the septum magnet. The result is a high-resolution, missing mass determination for $dd \to \alpha$X.

The entire system of channel and Pb-glass π^0 detectors was commissioned by observing the $pd \to h\pi^0$ reaction at several energies just above its threshold energy of 198.7 MeV. The recoil ^{3}He cone was matched in size to what we expected for the $dd \to \alpha\pi^0$ process. As described in Sec. III, this strong signal was used to check the energy of the Cooler beam based on its known reaction Q-value. It also provided a high-statistics means to optimize the operating values of the channel magnets and to measure the π^0 detection efficiency of the Pb-glass arrays.

Production running was scheduled across two months in the summer of 2002 with a break of several days in the middle. During the break, we chose to raise the beam energy from 228.5 to 231.8 MeV, thereby increasing the

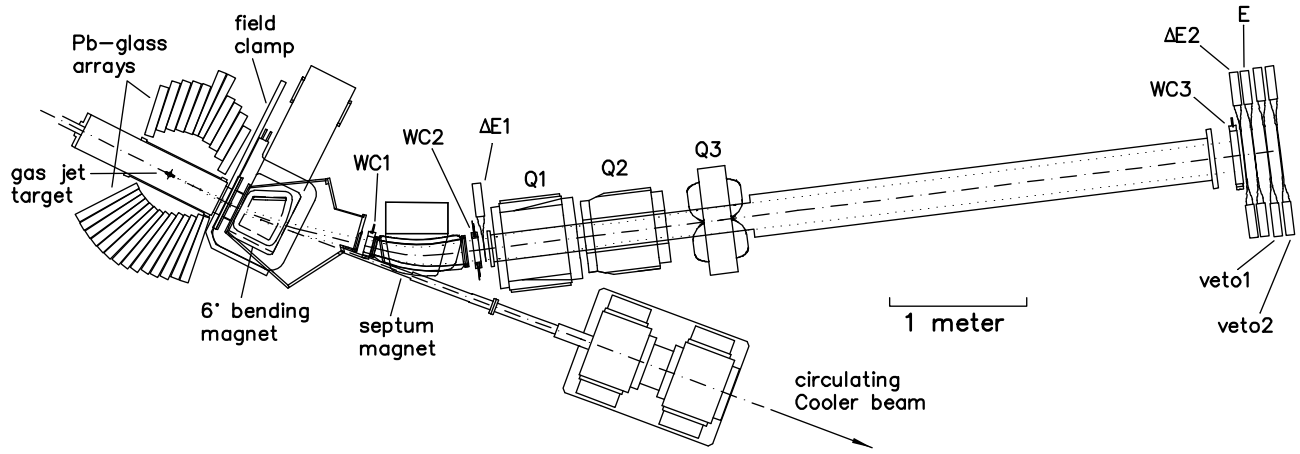

FIG. 1. Layout of the experimental setup showing the target, approximate locations of the Pb-glass arrays, and the magnetic channel in relation to a segment of the electron-cooled storage ring. Quadrupole magnets (Q1, Q2, and Q3), wire chambers (WC1, WC2, and WC3), and scintillation trigger (ΔE1, ΔE2, and E) and veto (V1 and V2) detectors are shown. The luminosity monitor detectors are small and consequently are omitted here.

recoil ^{4}He cone half-angle from 1.20° to 1.75° and the kinematic endpoint for $dd \to \alpha\gamma\gamma$ events from 135.0 to 138.0 MeV. The fact that the π^0 peak in the missing mass plot remained fixed while the $dd \to \alpha\gamma\gamma$ spectrum now extended to a higher energy became an additional confirmation of the analysis procedure, as intended, despite the fact that part of the recoil ^{4}He cone now fell outside the acceptance of the magnetic channel. The measurement of a total cross section at two energies also provided a crude check on the energy dependence that proved to be consistent with S-wave pion production.

In addition to proper and unambiguous identification of $dd \to \alpha\pi^0$ events, our experiment required a means of converting the extracted yields to absolute cross sections. Doing this with a circulating beam and a gas jet target necessitates the design and calibration of reliable monitor systems that provide an accurate measure of the cumulative luminosity for each of our measurements.

In the discussion that follows we provide a more detailed description of the various components of our experimental apparatus.

B. Beam

The preparation for deuteron beams at the IUCF involved installation of a new drift tube section tuned for deuterons in the injector linac and development of intense, unpolarized deuteron beams in the IUCF Cooler ring. The Cooler was well-suited to this experiment for several reasons. Its variable energy with narrow spread was essential for such near-threshold work. Electron cooling allows the use of thin internal targets, which prevents beam particles from being scattered into detectors at small angles to the beam. Also, one of its straight sections was designed with a nominal 6° bend as part of the lattice. This was used for the initial separation of the recoil alpha particles from the beam.

For this experiment, we used the highest beam intensity available, which was 1.5 mA. This value was limited by the space-charge expansion of the beam and the acceptance of the Cooler Ring. The Cooler operated with a beam cycle that took roughly 2.5 min. First, 10–15 deuteron beam bunches were injected into the storage ring from the Cooler Injector Synchrotron at 110 MeV. The bunches were cooled into a single bunch, then the ring energy was ramped to the operating point for the experiment near 230 MeV. Finally, data were acquired for about a 100 s interval for each cycle.

C. Target

1. *Gas jet/Target box*

While the use of a gas jet target was expected to greatly reduce many sources of background events, its use required high pumping speed in each of a series of baffled chambers surrounding the target. The required pumps (mechanical, cryopumps and turbopumps) obstructed much of the solid angle above and below the tall, narrow target box. Within the target box there was a series of three differentially pumped stages, each separated from the next along the beam by a thin aluminum foil with a square opening about 2.5 cm on a side, as shown in Fig. 2. Subsequent to running the experiment

we learned that the edges of some ^{3}He and ^{4}He recoil cones intersected these foils and it was necessary to include additional energy loss corrections in the analysis.

The glass nozzle was cooled by a copper cold head to 40 K. Most of the gas was collected and pumped away in the first two stages using high-speed mechanical pumps with the rest being collected on cryopumps in the vicinity of the target. The target nozzle emitted gas from below the beam, creating a column with an intense central core (about 2/3 of the gas) and a diffuse periphery (about 1/3 of the gas). Since this periphery fell away over a distance that was about equal to the distance to the first vacuum baffle in the differentially pumped vacuum system, it was necessary to develop a set of detectors that would determine the parameters of the gas-beam interaction region continuously during the course of the experiment.

2. *Target profile monitor*

To measure the spatial parameters of the gas-beam interaction region, we installed a forward pair of passing scintillator detectors that looked at deuterons scattered near $\theta_{\rm lab} = 5.4^\circ$ in coincidence with a position-sensitive silicon detector mounted inside the target box to catch the low-energy recoil deuterons. This system provided, through the position sensitivity of the silicon detector, a measurement of the target distribution along the beam axis. Since the parameters of this distribution depended on the operating parameters of the gas jet (mainly the pushing pressure), it was used for all of the production and calibration runs.

The scattering plane for this target profile monitor system was tilted at 24° to the horizontal plane to reduce the shadow of the silicon detector assembly on the left hand Pb-glass array while avoiding interference from the cold head holding the gas jet target nozzle. The silicon detector [33] had a single-axis, resistive-position readout that divided the signal charge according to position parallel to the beam direction. A front collimator restricted the acceptance in azimuthal angle to $\Delta\phi = 2.3^\circ$ about the tilted reaction plane. The silicon detector was cooled to reduce noise.

Deuterons going in the forward direction passed through the 6° magnet field used to separate the recoil ^{4}He nuclei from the $dd \to \alpha\pi^0$ reaction from the circulating deuteron beam. Since the forward scattered deuteron momenta were close to the momentum of the beam, the bend angle for both was similar. The forward scattered deuterons also passed through a vacuum baffle and a thick magnet vacuum box wall before hitting two scintillators. The first was 0.64 cm thick, with transverse dimensions of 2.54 cm × 2.54 cm. The second, lined up 15 cm behind the first, was 4.13 cm thick, with transverse dimensions of 2.54 cm × 2.62 cm. Although these scintillators were not thick enough to stop the elastically scattered deuterons, they provided good pulse height signals permitting unambiguous identification of the deuterons of interest. In addition, running them in a tight coincidence allowed us to eliminate much of the counting rate coming from other nearby sources.

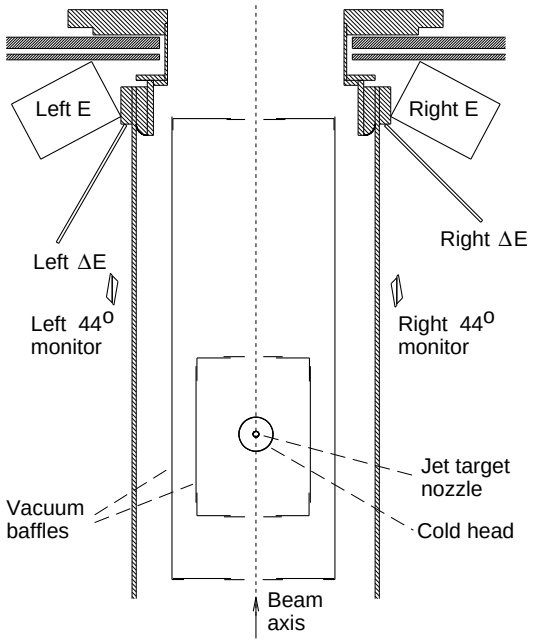

FIG. 2. Cross-sectional view through the mid-plane of the target box, showing two pumping stages with holes for the beam entrance and exit, the target box walls, left and right monitor scintillators, and left and right deuteron recoil detectors for the luminosity calibration. The two circles in the center are below beam height and represent the outer size of the gas jet nozzle and the cold head. Just behind the calibration stopping detectors are the two walls of steel used as field clamps for the 6° separation magnet. The 44° detectors observed $d + d$ elastic scattering coincidences. Each also operated in coincidence with an opposite side 25° system to observe $d + p$ elastic scattering (using an HD target). The left and right ΔE-E telescopes were removed whenever the Pb-glass arrays were rolled into place.

3. *Luminosity monitor*

In order to obtain a value for the total reaction cross section, we developed a monitor system to connect the response of our detectors to a suitable reference reaction of known cross section. In a storage ring like the Cooler, the event rate depends on the luminosity which is the product of the beam current and the amount of target intercepted by the beam. Since both the beam current and the target thickness vary with time and we could not

measure them independently, a quantity proportional to the product must be recorded and also calibrated. We divided this process into two stages, the monitoring of the luminosity during production running (so that its integral could be measured) and the calibration of that monitor against some other reference process whose cross section we knew from independent measurements.

As the monitor, we chose $d + d$ elastic scattering at $\theta_{\rm c.m.} = 90°$. To observe this, we placed small scintillation detectors at $\theta_{\rm lab} = 44.2°$ on the left and right sides of the gas jet target, as shown in Fig. 2. Operating at the ends of long, thin light guides, these scintillators were intended to minimize interference with the observation of photons from π^0 decay. The 44.2° detectors did not stop the scattered deuterons. Their pulse height signals gave dE/dx information useful for particle identification.

Several features were added to permit some horizontal and vertical information to be obtained. Each 44.2° detector was split along a diagonal and the light from the two halves routed through plastic light guides to separate photomultiplier tubes [34]. The changing relative thickness was used to yield information on the point where the particles passed through the detector. The side faces were cut at 45° to approximate a line projecting back to the target, thus providing a sharper edge to the detector acceptance. Each detector was 3.81 cm high. Also, the front detector was raised, and the rear one lowered, by 0.64 cm relative to the horizontal plane of the beam so that single hit events above and below could be used in checking the vertical alignment of the beam.

For the calibration of the monitor, we chose to make the cross section comparison between the $d + d$ elastic monitor reaction and the $d + p$ elastic reference reaction using a molecular HD gas target. Two additional scintillation detectors (a ΔE and E combination) were placed on both the left and right sides of the beam near 25° to capture deuterons that were in coincidence with 44.2° protons on the opposite side of the beam (see Fig. 2). The heights of the ΔE and E detectors were 5.08 and 7.62 cm respectively. Both of the sizes are larger than the nominal 2.54-cm overlap while their distance from the line of the deuteron beam is similar. This cross-calibration procedure is described in more detail in Section IV.

D. Gamma Detectors

Gamma detectors were required to identify those recoil events that were associated with one or more high energy gamma rays. Pb-glass Cerenkov counters were selected both because of their ability to contain the shower of one of our high energy gamma rays (typically 70 MeV) and because of their relative insensitivity to the large fluxes of deuterons, protons and neutrons from the circulating beam and the target region. The choice of modular arrays that were close to the target region on both sides of the beam (see Fig. 1) did allow us to identify two-photon events cleanly.

1. Elements/Modules

Two types of detectors were incorporated into this array, 160 IUCF detectors and 90 ANL detectors. The 160 IUCF detectors were built around 1985 for a proton-antiproton annihilation experiment at CERN's LEAR facility [35]. They were brought to IUCF and were used most recently in an $np \rightarrow d\gamma$ experiment [36]. The tapered blocks of Schott F2 glass (density = 3.61 g/cm^3) measured 4.2 cm × 6.4 cm on the front face, 6.4 cm × 6.4 cm on the back face, and 50 cm in length, compared with an attenuation length of 5.6 cm for a gamma ray energy of 70 MeV. Each block was attached to an EMI 9839B photomultiplier tube that contained 12 dynodes. Each block was wrapped with light tight material and its phototube was surrounded by individual magnetic-shield material.

The 90 ANL detectors were on loan (via Hal Spinka) from Argonne National Laboratory. They were originally constructed around 1970 for experiments E306 and E316 at the Argonne ZGS [37, 38]. They were upgraded for use in Fermilab experiment E704 in the early 1990's [39]. The rectangular blocks of Ohara optical glass (density = 3.85 g/cm^3) measured 6.4 cm × 6.4 cm and were 34.3 cm in length, compared with an attenuation length of 4.9 cm for a gamma ray energy of 70 MeV. Each block was attached to an Amperex 56AVP photomultiplier tube that contained 10 dynodes. The Pb-glass blocks and phototubes were encased in thin rectangular cans (for mechanical strength) that also included several layers of cylindrical magnetic shields of mu-metal about each phototube.

A cosmic ray test stand was set up to evaluate the performance of all of the Pb-glass detectors prior to the assembly of the two large arrays. About one-fifth of the older ANL detectors had to be refurbished, but eventually all of the detectors met our resolution and dark noise criteria.

2. Basic electronics/Cosmic ray monitors

The output of each Pb-glass detector was fed to a fast amplifier with dual outputs. One output was routed to an individual, charge-integrating ADC, providing independent pulse height information for each detector. The other output was routed to a fast, leading-edge discriminator and latch, which set a bit for each detector that fired its discriminator. The 250 discriminator outputs were multiplexed into 32 TDCs. The multiplexing was done in such a way that time information from nearest neighbors in an array could be distinguished with no ambiguity. Ambiguities with next nearest neighbors could be resolved in almost all cases by using the bits set by the discriminators of each detector fired.

Initially, the HV of each detector was set to give a cosmic ray peak at about channel 500. At this gain, the lower-level discriminators could be set at about 8 MeV. All Pb-glass detectors with data were recorded with each

event even though this information was not used in the trigger. This allowed us to study offline the effects of time and energy thresholds at a higher level in the analysis phase of the experiment.

Because of the low rate of $dd \rightarrow \alpha\pi^0$ events (a few/day), we needed an independent monitor of the performance of the Pb-glass detectors. Long (in the beam direction) scintillator trigger detectors were placed above and below each of the Pb-glass arrays to initiate a readout whenever there was a cosmic muon that passed through these cosmic ray trigger detectors. At the beginning of a long run, this provided a way to match the gains of all of the Pb-glass detectors. During the course of each long run, it also provided a way to check each array for performance issues. During production running, the Pb-glass detector gains were updated daily. As a result of these periodic checks, in the final analysis only 8 of the 250 detectors had to be discarded.

3. Performance of Arrays

The Pb-glass modules were stacked in two close-packed arrays. The arrays were constructed to give a roughly constant radius from the intersection of the beam with the gas jet and the closest point on the detectors. The array on the right side of the target was composed entirely of IUCF detectors, arranged in 10 layers, each with 14 modules. Four "dummy" detectors were added to the right array to make the total number of modules a multiple of 16 (144 total). The array on the left side of the target had 10 layers, each with 11 modules. Two of the central columns of the left array were IUCF detectors, the rest were ANL detectors. Two "dummy" detectors were added to the left array to make the total number of modules a multiple of 16 (112 total).

The overall time resolution of each array was about 0.8 ns, yielding a gamma-gamma coincident time peak with a FWHM of about 1.1 ns. This provided an excellent mechanism for identifying events associated with two high energy photons. The summed pulse height signals in each array yielded well-defined peaks for the photons associated with the events of interest. The FWHM resolution for the right array was about 40% for 70 MeV photons, and the FWHM resolution for the left array was about 50%. With such resolution we were able to run the detectors with the discriminators set well above the noise level of the photomultiplier tubes, with only a small loss in photon detection efficiency. (See Sec. III.C.)

The arrays afforded a moderate measure of angular resolution as a result of their modular construction. The angular resolution and pulse height resolution of the two arrays were insufficient, however, to provide by themselves a useful determination of missing mass that could be applied in the analysis for identification of the π^0 production channel.

The recoil ^{4}He nuclei from $dd \rightarrow \alpha\pi^0$ events and from $dd \rightarrow \alpha\gamma\gamma$ events that were within the acceptance of the downstream magnetic channel had photon distributions that were indistinguishable to our arrays. This would have remained the case even with an order of magnitude improvement to our angular resolution for gamma rays. Hence, the separation of $dd \rightarrow \alpha\pi^0$ and $dd \rightarrow \alpha\gamma\gamma$ events had to be carried out using information from the magnetic channel exclusively.

E. Magnetic Channel

Near threshold it becomes possible to fit all of the recoil ^{4}He nuclei within the acceptance of a downstream magnetic channel. In a transverse magnetic field our charge-two ^{4}He recoils were bent about twice as much as the charge-one deuteron beam, so the separation of the recoils from the circulating beam was easy. However, distinguishing $dd \rightarrow \alpha\pi^0$ events from $dd \rightarrow \alpha\gamma\gamma$ events was much more difficult. Since this identification of the final state relied entirely on suitably precise measurements of the four-momentum (i.e., vector momentum and energy) of the ^{4}He recoils by the detectors in this magnetic channel, simulations of the channel performance prior to its construction were essential. The important components of the magnetic channel are shown in Fig. 1.

1. 6° bending magnet/Septum magnet

The first dipole magnet (nominally a 6° bending magnet for the beam) provided a uniform field over a fairly wide area of scattered particles and had a 12.7 cm gap between the pole faces. Since its magnetic field ramped with the other Cooler ring magnets from injection at 110 MeV up to 230 MeV, a field clamp on the upstream side was required to shield the Pb-glass detectors from rapidly changing magnetic fields. The 6° bending magnet bent the ^{4}He recoils by 12.5° on average, so the axis of the recoil cone diverged from the deuteron beam at an angle of 6.5° after this dipole.

The angular size of the recoil cone grows like the square root of the energy available above threshold (T_d−225.5 MeV). Since the predicted cross section also increases, the goal was to design a magnetic channel with the largest useful aperture which preserved good optics. The largest aperture focusing magnets available to us had about a 20 cm bore. At the closest possible location, this corresponds to a maximum recoil cone half-angle of about 1.7° or a deuteron energy about 5.5 MeV above threshold. If the cone half-angle is 1.7°, the alphas will just become spatially separated from the (very small) deuteron beam at a distance of 30 cm past the center of the 6° bending magnet. In another 40 cm, they will be separated by enough distance to accommodate a beam pipe and vacuum window frame. If the alpha cone were allowed to continue to expand over the 6 m flight path (for the TOF measurement), it would grow to 45 cm in diameter neglecting further angle spread caused by the ΔE1

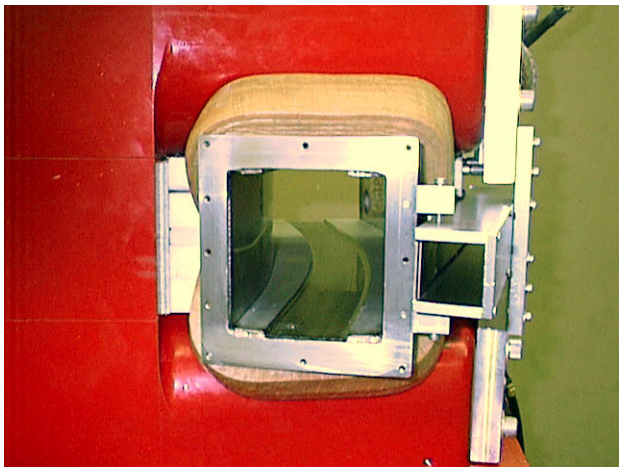

FIG. 3. A view of the entrance to the septum magnet. The large channel that curves to the left is for recoil ^{4}He. The field windings are located inside the red form around this channel. The insulated windings appear as tan in the picture. The smaller square channel to the right is for the circulating deuteron beam in the Cooler ring. Note that the windings dip and travel in between the ^{4}He channel and the beam pipe, thus keeping the stray field low in the vicinity of the beam.

detector used to start the timing.

To keep the alpha cone small, the dipole septum magnet began as close to the exit of the 6° bending magnet as possible. Its magnetic field strength (15.2 kG) provided enough of a bend angle (24.6°) that the channel focusing elements (Q1, Q2, and Q3) could clear the Cooler ring quadrupole. In order to initiate the focusing function of the magnetic channel as soon as possible, the field edges of the septum magnet were angled to provide vertical focusing of the alpha cone. Finally, when moving horizontally outside the pole face gap, the magnetic field must be reduced to the order of 1 G in order that the nearby stored Cooler beam not be adversely affected. Characteristics of the final septum magnet design were calculated with the finite element code MagNet [40]. A front view of the septum magnet is shown in Fig. 3.

The septum magnet required a large current density. The C-shaped yoke, with a pole face gap of 12.7 cm, produced a flat dipole field with edge angles set to 22° each. The coils were designed to pass between the deuteron and recoil beams so that there would be little residual field along the axis of the Cooler beam line. Only small additional field clamps were needed to provide sufficient stray field suppression. The predicted shape of the fringe fields were used to design magnetic shielding to protect the circulating Cooler beam.

2. *Quadrupole magnets/Drift pipe*

All of the detectors, both scintillators and wire chambers, were operated in air. We found it advantageous in order to minimize energy losses to build vacuum channels inside the septum magnet and in the channel straight section that ran from the inlet of the first quadrupole magnet to the final detector stack. Each vacuum window was made of thin Kapton [41]. At the exit of the 6° bending magnet there was a 5 mil Kapton foil to insure the vacuum integrity of the Cooler system. Due to its large size, the exit window of the channel straight section was also sealed with a 5 mil Kapton foil. The other three vacuum windows in the magnetic channel were made of 3 mil Kapton foils.

The channel quadrupole triplet (in which the center magnet was vertically focusing) was used to focus the recoil cone on the downstream detectors. However, the size of the recoil cone on these detectors resulted more from multiple scattering in the detector system than from the quality of the optical focus. Losses and optical properties along the channel were monitored by two additional wire chambers - one at the entrance to the straight section of the magnetic channel and the other at the exit.

3. *Detectors in the magnetic channel*

Triggering and time of flight (TOF) measurements were accomplished with plastic scintillators. The first of these, ΔE1, was very thin (0.8 mm) and located just after the septum magnet. The scintillator was divided into four quadrants, each with its own PMT, in order to reduce the singles rate in each part. Two thicker scintillators, ΔE2 (3.2 mm) and E (3.2 mm), were located at the end of the channel. The thickness of the E detector was determined so that ^{4}He recoils from the $dd \rightarrow \alpha\pi^0$ reaction just stopped in this detector. The flight path between ΔE1 and ΔE2 was made as large as possible (5.7 m) in order to determine the recoil TOF with sufficient precision. Each scintillator at the end of the channel had two photomultiplier tubes, one on the left and one on the right. This made it possible to do mean timing across these large pieces (20.3 cm high × 35.4 cm wide).

The detectors in the channel were required to accomplish three tasks. First, recoil ^{4}He (or ^{3}He) events were identified by their energy loss in the series of three plastic scintillators (ΔE1, ΔE2, and E in Fig. 1). Second, the z-component of the recoil momentum was measured using time of flight between the first scintillator (ΔE1) located between the septum magnet and the quadrupole triplet and the scintillator pair at the end of the channel (ΔE2 and E) some 6 m downstream. Third, the transverse momentum component of each recoil was calculated from a measurement of its scattering angle by a wire chamber (WC1) with 2 mm wire spacing located just in front of the septum magnet where there would be minimal distortion from bending in magnetic fields. Two additional wire chambers [WC2 (2 mm spacing) and WC3 (4 mm spacing)] were placed at the position of the ΔE1 scintillator and at the end of the channel, respectively, to monitor the performance of the channel. Two back-to-back veto scintillators (Veto1 and Veto2 in Fig. 1), each

6.4 mm thick, mounted directly behind the E scintillator were used to eliminate any charge-one particles making it to the end of the channel.

Protons were expected in copious numbers because the rigidity of breakup protons from beam deuterons matches the rigidity of the recoil ^{4}He nuclei. Thus particle ID played an important role in separating charge one particles (protons and deuterons) from charge two particles (^{3}He and ^{4}He nuclei).

F. Electronics and Event Types

HV supplies, fast amplifiers, individual ADCs, leading-edge discriminators, and multiplexed TDCs were all located in the Cooler vault close to the gas-beam interaction region and the magnetic channel. Fast event-by-event recording was buffered to handle the high rates. This allowed us to achieve an overall left-right, two-gamma coincidence time resolution of about 1.1 ns FWHM. Fast timing was also crucial in the operation of the scintillation detectors in the magnetic channel. Here, in order to obtain a good missing-mass resolution, we required a FWHM of 0.2 ns for the ΔE1-ΔE2 TOF.

Because of its ability to strongly filter charge one particles coming from the interaction region, our "magnetic channel events" stream was initiated by particles which made it to the end of the magnetic channel (i.e., fired ΔE1, ΔE2, and E in coincidence) and did not fire either veto detector. The coincidence timing was set to include charge two recoils and to avoid the bulk of the faster protons in the channel. Since events of interest were identified by the magnetic channel detectors and they were downstream of the interaction region by up to 10 meters, the gamma ray signals had to be delayed substantially (using low-loss coaxial cable) in order to be available for processing when a suitable recoil event was identified in the magnetic channel. This relatively simple event trigger permitted a wealth of diagnostics to be made, among them the determination of the efficiency of the wire chambers for charge two recoils.

The detectors described above allowed us to record the following types of events simultaneously:

(1) Magnetic channel events: prescaled events in which ΔE1, ΔE2, and E fired in coincidence, and neither veto scintillator fired. The coincidence timing was set to include charge two recoils and to avoid the bulk of the faster protons in the channel. This kept the un-prescaled trigger rate below 1000 s^{-1}, making production running possible without a more restrictive trigger.

(2) Potential CSB events: events in which ΔE1, ΔE2, and E and at least one Pb-glass Cerenkov detector fired in coincidence, while neither veto scintillator fired. The coincidence timing was set to include prompt gammas associated with magnetic channel events.

(3) Random CSB events: these events were identical to CSB events, but with the coincidence timing set to a window on gammas that did not include prompt coincidences.

(4) Cosmic ray muon events: events for which there was a coincidence between the scintillator detectors placed above and below each of the Pb-glass detector arrays. The coincidence timing was set to correspond to fast cosmic ray muons passing vertically through the trigger scintillators.

(5) Luminosity monitor: prescaled events in which either of the two luminosity scintillators on one side of the target was in prompt coincidence with either of the luminosity scintillators on the other side of the target.

(6) Target profile monitor events: prescaled events in which a tight coincidence was required of the two plastic scintillators mounted downstream of the 6° bending magnet, and then this signal was set in coincidence with the position sensitive silicon detector mounted near the target.

(7) Scaler events: scalers were set up to be read out every 10 s.

G. Data Acquisition

Once the ramped Cooler beam was stable, a valve was opened to allow the target gas to flow and then data acquisition began. The target scattered particles out of the beam causing the intensity to drop at a fixed rate. After about 100 s, data acquisition stopped, the target was turned off, the beam was dumped, and the Cooler magnets were reset for the next injection/ramp cycle. When the target valve was open, gas at a certain preset pushing pressure flowed through a cooled glass target nozzle.

We conducted production running and luminosity calibration running at different operating pressures for the gas jet target. For production running, we maximized the throughput of events in the data acquisition system as a function of the beam lifetime and the time that the beam was held at full energy in the Cooler ring. The lifetime was a function of the thickness of the gas jet target. The most efficient operation came with a beam lifetime of about 100 s. This value was controlled by changing the pushing pressure ahead of the glass target nozzle. In this configuration, we prescaled the event rate for the luminosity system to reduce the dead time of our data acquisition.

For the luminosity calibration, it was important that we conserve the molecular HD gas and use as large a fraction of the available luminosity events as possible. In this situation, the pushing pressure for the target nozzle was reduced to lower the gas flow (see Sec. IV).

III. COMMISSIONING OF EXPERIMENTAL APPARATUS

Prior to CSB production running, a great deal of new apparatus had to be brought on line and its properties in-

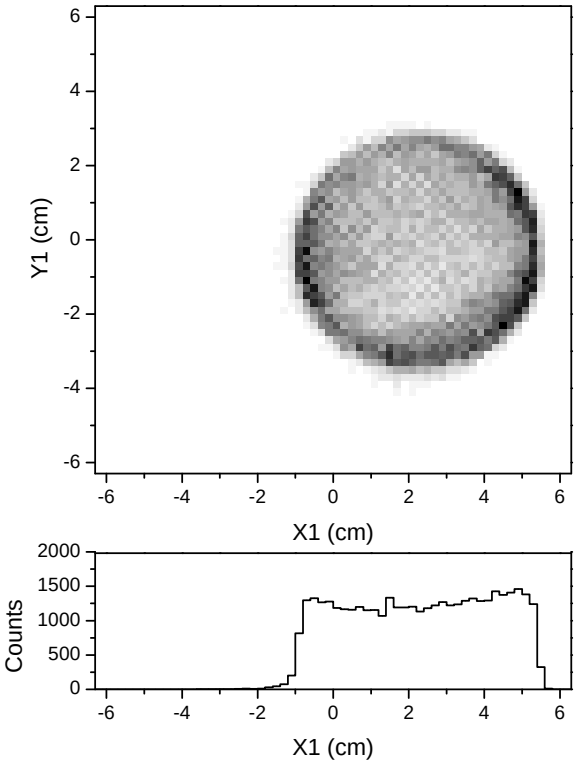

FIG. 4. ^{3}He recoil distribution in wire chamber WC1 for the $pd \rightarrow h\pi^0$ reaction at 200.2 MeV. (top) The 2-D plot shows the locus of events produced by a 1.45° opening cone of ^{3}He recoils. (bottom) The projection onto the X-axis shows a distribution with sharp edges.

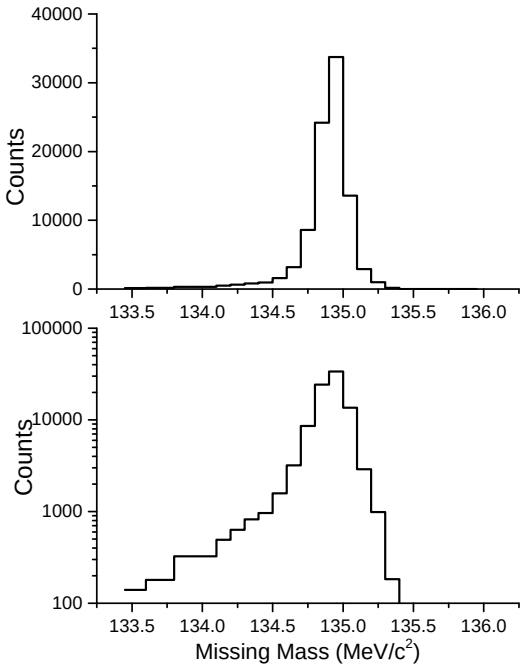

FIG. 5. Two views of the reconstruction of the $pd \rightarrow h$X reaction ^{3}He recoil missing mass with a linear plot on top and a logarithmic plot on bottom. The data were obtained using the magnetic channel elements set for the 0.95° ^{3}He recoil cone from the $pd \rightarrow h\pi^0$ reaction at a proton beam energy of 199.4 MeV. The π^0 peak at 135 MeV/c^2 has a FWHM of 240 keV.

vestigated and measured. The near-threshold $pd \rightarrow h\pi^0$ reaction was chosen for these tasks with a proton beam incident on a deuteron target. The cross section for this reaction is well-known and relatively large ($\sim 1\ \mu b$) near threshold [32, 42, 43]. The kinematics near threshold for this reaction provide ^{3}He recoils and photons that are well-matched to those of the CSB reaction, making it possible to perform useful measurements with minimal modifications to the apparatus. The $pd \rightarrow h\pi^0$ reaction provided an effective means of tuning the magnetic channel, making a precise calibration of the Cooler beam energy, and making a direct determination of the π^0 detection efficiency of the Pb-glass detector arrays.

A. Tuning the Channel

One of the main differences between the ^{3}He recoils from the near threshold $pd \rightarrow h\pi^0$ reaction and the ^{4}He recoils from the near threshold $dd \rightarrow \alpha\pi^0$ reaction is that the ^{3}He recoils have less range in scintillator material. The primary trigger (CSB events) was modified to require a signal only in ΔE1 and ΔE2. A signal in the E detector was not required. Removing the requirement of a coincident photon approximately doubled our event rate, thereby facilitating tuning the channel.

The signals from the $pd \rightarrow h\pi^0$ reaction were very clean and demonstrated that the channel performed as designed. Figure 4 shows the distinctive locus of events seen in wire chamber WC1 produced by a 1.45° opening cone of ^{3}He recoils. The extremely low level of background is better illustrated in Fig. 5, which shows a reconstruction of the π^0 missing mass. The missing mass is computed using conservation of energy and momentum, the beam energy determined from the measured Cooler circumference and the Cooler RF frequency, as well as the ^{3}He recoil's momentum and energy obtained from the magnetic channel. The reconstructed π^0 missing mass was chosen as the variable to best distinguish $dd \rightarrow \alpha\pi^0$ events from $dd \rightarrow \alpha\gamma\gamma$ events. Our work with the $pd \rightarrow h\pi^0$ data showed that this reconstruction worked well, providing a FWHM resolution of 240 keV. These data provided a means to determine ways to optimize the missing mass resolution and to investigate factors leading to its deterioration.

Another difference between the tuning reaction $pd \rightarrow$

$h\pi^0$ and the CSB $dd \rightarrow \alpha\pi^0$ reaction is that the recoil ^{3}He nuclei have less rigidity in the magnetic field. As a result, the field settings for the ^{3}He recoils were different than those needed for the CSB ^{4}He recoils. We found that the optimal settings for the ^{3}He recoils were very close to the design values.

The energy losses of the two types of recoils in the various materials in the magnetic channel were different and needed to be carefully accounted for in setting up the coincidence timing between the ΔE1 and ΔE2 scintillators. The $pd \rightarrow h\pi^0$ runs provided a means to test and tune our handling of energy loss in the channel, and its effect on measured time of flight between ΔE1 and ΔE2. This also had a direct impact on our determination of the π^0 missing mass.

The information obtained from the $pd \rightarrow h\pi^0$ runs was used to *calculate* the field settings needed for the $dd \rightarrow \alpha\pi^0$ production runs, and to *calculate* the necessary changes in trigger timing for those events. Production running started with no independent confirmation that these were correct except for the observation of a $dd \rightarrow \alpha\pi^0$ signal. Things worked as predicted, except for the zero offsets used in each of the four legs of the time of flight system. These legs came from the segmentation of the ΔE1 detector into four quadrants, each with its own photomultiplier. It was necessary to change photomultiplier voltages on the ΔE1 and ΔE2 scintillators to bring the ^{4}He recoil pulse height signals within a useful operating range. Because of this, as will be described later, it was necessary to find new timing offsets for the $dd \rightarrow \alpha\pi^0$ analysis.

B. Energy Calibration

In order to reconstruct the missing mass using information obtained from the magnetic channel, it is essential to have a precise and accurate value for the incident beam energy. A beam stored in the Cooler has a period that is given by the inverse of the Cooler RF frequency, which is measured to an accuracy of better than ± 10 Hz (out of a few MHz). A beam stored in the Cooler also has an orbital path that is strongly constrained, resulting in a circumference that is well determined. Using the Cooler circumference and the Cooler RF frequency, one can obtain the speed of the beam particles, and hence the beam energy, to very high precision.

The determination of beam energy by this means relies on a precise measurement of the Cooler circumference. This can be obtained by using a calibration reaction that provides an independent means of determining the beam energy. The $pd \rightarrow h\pi^0$ reaction is a very effective calibration tool because the opening cone angle of the recoil ^{3}He varies rapidly near threshold. One finds near threshold that the incident beam energy varies as the square of the cone angle θ :

$$T_p = T_{th} + \alpha\theta^2 \qquad (3)$$

where the threshold energy $T_{th} = 198.738$ MeV, the proportionality constant $\alpha = 0.701$ MeV/deg^2, and the angle θ is in degrees.

A precise measurement of the width of the cone can be made using the first wire chamber (WC1) in the CSB magnetic channel. This wire chamber is positioned very close to the exit of the 6° magnet. The pattern of ^{3}He hits on this detector is the most direct measurement of the maximum scattering angle, because the cone emerges from vacuum for the first time only a few centimeters before entering this wire chamber. Hence, any multiple scattering effects from the window and air traversed are minimal. We performed a series of calibration measurements at six Cooler RF frequencies that are summarized in Table I.

In Fig. 4 is shown the locus of events in WC1 associated with a cone angle of 1.45°. One finds that the horizontal X and vertical Y projections of this distribution have very sharp edges. The width of the projection is the distance between the half maximum points for each edge. We estimate a random uncertainty of ± 1.0 mm in the measured width of each projection for each of our measurements. Due to a small amount of vertical focusing from the 6° magnet, one observes a reduction in the vertical width of typically 4%, as illustrated in Table I.

One obtains a good first determination of the cone angle using the average of the widths, suitably corrected for vertical focusing, and the path distance from the target to the center of the locus (124.0 ± 0.3 cm). Part of the uncertainty in the path distance comes from the width of the gas jet (± 0.2 cm) and part from the uncertainty in the physical measurement (± 0.2 cm). Using this determination of the cone angle as a starting point, calculations using the beam-optics program TRANSPORT [44] were performed to find the cone angle that produced the best fit to the measured widths. These results are tabulated in the fourth column of Table I. The uncertainty in these results (± 0.025°) is dominated by the uncertainty in the measured widths obtained from WC1.

Using the cone angle θ, the associated beam energy T_p was determined and is tabulated in column five of Table I. From this energy, the speed of the protons was computed and finally the working circumference of the Cooler was determined. These results and their uncertainties are tabulated in column six of Table I. The weighted average of the measurements of the Cooler circumference is 86.7864 ± 0.0023 m. Using this value and the Cooler RF we calculate what we call the actual beam energy T_p^*, and tabulate it in column seven. These energies each have a propagated uncertainty of ± 14 keV. The last column of Table I is the deviation between T_p^* and T_p. The circumference of the Cooler plays an essential role in the determination of missing mass.

TABLE I. Determination of Cooler circumference using the reaction $pd \to h\pi^0$. Horizontal and vertical widths of the recoil cone, from WC1, are in columns two and three. The cone angle is determined from these widths. The proton beam energy and Cooler circumference are calculated and the weighted average of these circumferences is used to compute the calibrated beam energy in column seven. The difference between this energy and individually determined beam energies is in column eight.

Cooler RF freq (MHz)	Horizontal X width (cm)	Vertical Y width (cm)	Cone angle θ (deg)	Beam energy T_p (MeV)	Cooler Circumference (meters)	Beam energy T_p^* (calib) (MeV)	Deviation $T_p^* - T_p$ (keV)
1.95210	2.76	2.65	0.629	199.015 ± 0.022	86.788 ± 0.0036	199.006	-9 ± 26
1.95314	3.90	3.78	0.893	199.297 ± 0.031	86.787 ± 0.0050	199.290	-7 ± 34
1.95401	4.72	4.47	1.077	199.551 ± 0.038	86.790 ± 0.0062	199.529	-22 ± 40
1.95575	5.83	5.50	1.325	199.969 ± 0.046	86.780 ± 0.0074	200.006	$+37 \pm 48$
1.95660	6.45	6.16	1.466	200.245 ± 0.051	86.787 ± 0.0082	200.239	-6 ± 52
1.95752	6.88	6.48	1.554	200.431 ± 0.054	86.776 ± 0.0087	200.492	$+61 \pm 56$
±0.00001	±0.10	±0.10	±0.025		Weighted mean 86.7864 ± 0.0023 m	± 0.014	Weighted dev 0 ± 16 keV

C. Photon Efficiency

The commissioning of the experimental apparatus provided an effective means of making a *measurement* of the π^0 detection efficiency of the Pb-glass arrays for the $pd \to h\pi^0$ reaction near threshold. Data were collected for approximately two days at a proton beam energy of $T_p = 199.404$ MeV. This energy provided a cone of ^{3}He recoils with a maximum angle of 0.95°, and a total cross section of about 1.0 μb [32, 42, 43]. These recoils traversed the magnetic channel with very few losses. The energy and angle spectra of the decay photons are comparable to those from the $dd \to \alpha\pi^0$ reaction near threshold. The absence of any appreciable background allows one to use these ^{3}He recoils as a means of tagging π^0's, and hence this scheme provides an experimental means to measure the efficiency of the Pb-glass arrays to detect those particles.

The use of an isotopically pure gas jet target with no windows gives rise to only two classes of intrinsic background in the ^{3}He recoils; $pd \to h\pi^0\gamma$ and $pd \to h\gamma$. The $pd \to h\pi^0\gamma$ reaction is expected to have a cross section about 100 times smaller than $pd \to h\pi^0$. In addition, very near the $pd \to h\pi^0$ threshold the additional gamma will have very low energy, and give rise to a negligible change in the energetics of the π^0, making this background virtually indistinguishable from $pd \to h\pi^0$ for our apparatus.

The $pd \to h\gamma$ reaction has a total cross section of 950 ± 100 nb at our beam energy, with most of the cross section in forward going γ rays [45, 46]. The cross section for $pd \to h\gamma\gamma$ is expected to be about 100 times smaller than that for $pd \to h\gamma$, or about 10 nb. This is about 1% of the $pd \to h\pi^0$ cross section. Almost all of this background will have reconstructed missing mass values less than 132 MeV/c^2, well outside the observed peak (Fig. 5).

The recoil cone for the ^{3}He recoils for the $pd \to h\gamma$ reaction has a maximum angle of 12.5°. Only the central part of this cone makes it through the nominal 1.7° acceptance of the magnetic channel. These events correspond to the most and least energetic of the recoils for that reaction. The least energetic recoils had insufficient energy to make it to the ΔE_2 scintillator. The most energetic recoils correspond to γ's emitted at very back angles. The cross section for such events integrated over the acceptance of the magnetic channel is $\sim$ 1 nb [45, 46]. This is $\sim$ 0.1 % of the $pd \to h\pi^0$ cross section. Both of these backgrounds are small relative to the size of the π^0 tagging peak. In addition, these recoils have a TOF significantly shorter than those associated with π^0 production, making their identification clear and unambiguous.

Particle identification (PID) in the magnetic channel was accomplished using the pulse height from $\Delta E2$ and time-of-flight (TOF) between $\Delta E1$ and $\Delta E2$. Histograms of TOF versus $\Delta E2$ pulse height show how ^{3}He and ^{4}He are cleanly separated using a tight two-dimensional gate around the ^{3}He group. ^{4}He particles, which might arise from beam striking heavy materials in the Cooler, are seen to be a negligible portion of the events making it through the magnetic channel in this $pd \to h\pi^0$ study.

Using angle information obtained from WC1 and TOF information from $\Delta E1$ and $\Delta E2$, the missing mass (MM) associated with the detected ^{3}He recoils was computed. Figure 5 shows that one obtains a narrow peak for the π^0's with a FWHM of $\sim$ 240 keV. To reduce physical background to negligible levels, a requirement that the MM be greater than 132 MeV/c^2 was imposed on particles falling in our PID window. Particles satisfying these conditions were used to provide "tags" of π^0 events. One sees in Fig. 5 that over 99% of these events were associated with π^0's.

A valid π^0 "hit" in the Pb-glass arrays required: at least one module in each array with a pulse height exceeding channel 124; a cluster summed pulse height in each array exceeding channel 249; and a TOF between

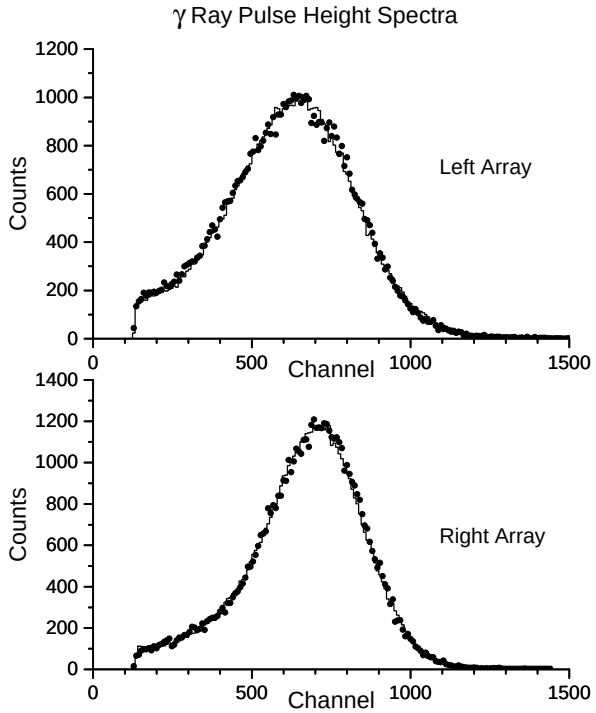

FIG. 6. Cluster summed pulse height spectra for the left (top) and the right (bottom) Pb-glass arrays obtained for events from the $pd \to h\pi^0$ reaction at a proton beam energy of 199.4 MeV. The points are the data, and the histograms are from the simulation of the experiment. The peak in the top panel corresponds to an intrinsic γ-ray energy of 68.5 MeV, and the peak in the bottom panel corresponds to an intrinsic γ-ray energy of 70.2 MeV. The majority of the width in each spectrum originates from the resolution of the Pb-glass modules.

the Pb glass module with the greatest pulse height on each side and $\Delta E1$ that fell within set gates.

Each module in the Pb-glass arrays had a discriminator with a threshold of 40 mV. The gains of the tubes were set to place a cosmic ray peak from the cosmic ray monitor near channel 500. Because we could not set PMT voltages precisely in the hardware, there was some variation in the effective hardware thresholds of the modules. However, these thresholds were all below channel 110, with a typical value of about channel 80, corresponding to an intrinsic γ ray energy of about 8 MeV. Small adjustments were made to the gains of the individual modules in the off-line analysis to put the cosmic ray peaks more precisely into channel 500.

A cluster summed pulse height was constructed in each array using signals from immediate neighbors of the module with the largest pulse height. Only signals exceeding channel 124 were included in this sum. Representative histograms of the resulting signals are shown in Fig. 6. One finds a well-defined gamma ray peak in the cluster summed pulse height spectrum for each Pb-glass array. The peak in the left array at channel 645 corresponds to an intrinsic γ ray energy of 68.5 MeV, and the peak in the right array at channel 710 corresponds to an intrinsic γ ray energy of 70.2 MeV. The intrinsic γ ray distributions for each array have a FWHM of about 23.3 MeV, or about 33%. The measured FWHM for the left array is 68% and for the right array is 50%. The majority of this width is due to the resolution of the Pb-glass modules. The width of the peak in the left array is somewhat greater than that in the right array because the Argonne modules used in the left array did not have as good an energy resolution as the IUCF modules.

An experimental efficiency for π^0 detection was obtained by dividing the number of events in the Pb-glass arrays satisfying the photon sorting conditions by the number of recoils "tagged" by the magnetic channel. This efficiency was examined as a function of the cluster sum threshold and it was found to be slowly varying with the cluster sum threshold. This is a consequence of the slowly varying, low energy tail of the cluster summed pulse height spectrum.

The measured π^0 detection efficiency for $pd \to h\pi^0$ at a beam energy of 199.404 MeV at the cluster sum threshold of 250 was 0.3526 ± 0.0015 (statistical). It should be noted that, because of the "tagging" technique used, this result is *independent* of the total cross section for $pd \to h\pi^0$. A Monte Carlo simulation of the experiment was used to compute the efficiency for π^0 detection in these $pd \to h\pi^0$ measurements. This calculation yielded an efficiency of 0.3567 ± 0.0015 (statistical) ± 0.0036 (systematic) which differs from the measured value by only 0.0043. The dominant contribution to the systematic error was the uncertainty in the small correction (2.2%) for losses due to corruption of the gamma time by other multiplexed modules going into the same TDC. The pulse height spectra generated by the simulation are also in excellent agreement with the data, as seen in Fig. 6. This provides an additional test of the accuracy of the calculations and of the model constructed to simulate the experiment.

IV. LUMINOSITY CALIBRATIONS

A. Overview

A measurement of the total $dd \to \alpha\pi^0$ cross section requires a value for the integrated luminosity during production running. We chose to scale the $dd \to \alpha\pi^0$ cross section relative to $d + d$ elastic scattering at angles near $\theta_{\rm c.m.} = 90°$. The two deuterons emerging from the target region at laboratory angles near $\theta_{\rm lab} = 44.2°$ were observed in coincidence by our luminosity monitor scintillators mounted to the left and right of the target as shown in Fig. 2.

Since the $d + d$ elastic scattering cross section has not

been measured in the vicinity of 230 MeV, it was necessary to conduct a second calibration measurement during the CSB production running in which the $d + d$ elastic scattering cross section was measured relative to the reference $d+p$ elastic scattering cross section. This comparison was made with a molecular HD target so that the areal densities of the deuteron and proton targets would be the same. As discussed below in Sec. IV.D, since $d+p$ reference cross section measurements also did not exist at the required energies and angles, an appropriate procedure was developed to extract them from published data.

B. Measurements

The cross section comparison required two additional scintillation detectors (a ΔE and E combination) to be added on both sides of the beam near 25° to capture deuterons that were in coincidence with 44.2° protons on the opposite side of the beam (see Fig. 2). In the 25° telescopes, the detectors could observe both $d+d$ and $d+p$ scattering. Discrimination of these two processes relied on a measurement of the energy of the recoil particle which is twice as large for the recoil proton.

Since the target was changed to molecular HD gas, we also took data with hydrogen (H_2) and deuterium (D_2) targets separately so that we would have template spectra for the two cases. For both $d + d$ and $d + p$ elastic scattering, it is possible to have deuteron breakup events that trigger the scintillator system. Separation of these events relied on a combination of dE/dx particle identification and background subtraction. To include the extra 25° detectors in our setup, we had to roll back each Pb-glass array during the calibration measurements. A track system was provided in the mounting design to facilitate this motion as well as to allow for target system maintenance.

The horizontal plane location of the 44.2° and 25° scintillation detectors is shown in Fig. 2. For the measurement of the $d + p$ cross section with this system, it was expected that the solid angle would be determined by the protons scattering into the detectors at 44.2° and that all associated deuterons would be captured by the detectors near 25°. In practice, the target distribution along the beam was long enough that some forward deuterons missed the scintillators because their trajectories fell between these detectors and the beam. A Monte Carlo model was used to calculate this geometrical loss. The reaction losses, which are different for protons and deuterons, were also taken into account (see Sec. V.C).

While the deuterium target thickness for production running was optimized to maximize the yield of $d + d$ data, during the calibration of the luminosity monitor the target operating pressure was changed in an effort to conserve the (expensive) molecular HD gas. These two operating points led to significant acceptance differences for the $d + d$ luminosity monitor. These differences were investigated using Monte Carlo simulations described in the next section.

C. Data Analysis

During calibration running, three separate coincidences could generate a trigger for the calibration detector arrangement corresponding to $d + d$ and two possible $d + p$ elastic scattering events: a left 44.2° and a right 44.2° coincidence; a left 25° and a right 44.2° coincidence; and a left 44.2° and a right 25° coincidence.

When the target pressure was reduced, the width of the distribution of target gas along the beam line became larger. This change was visible in the distribution of recoil events on the position sensitive silicon detector that was a part of the target profile monitor system. Figure 7 shows the distributions for production running (top) and luminosity calibrations (bottom). Both of the distributions were measured with pure deuterium gas in the target. The calibration of the length along the beam comes from the edges of the distribution imposed by the collimating slit in front of the position-sensitive silicon detector.

The two operating points for the gas-jet target led to significant acceptance differences for the $d+d$ luminosity monitor. As a result of measurements made using the target profile monitor system, we chose a model consisting of the sum of two Gaussian shapes. The narrow distribution corresponded to the gas jet and the wide distribution corresponded to a diffuse component of the target. The best fit curves for the distributions in Fig. 7 are included. The widths and relative sizes of these shapes remained stable during the course of the experiment. Thus we adopted average shapes for our simulation. For production running, the narrow and wide Gaussians had widths of $\sigma_< = 0.235$ cm and $\sigma_> = 1.28$ cm, and the narrow Gaussian contained 66.2% of the total area. For calibration running, the narrow and wide widths were $\sigma_< = 0.439$ cm and $\sigma_> = 1.59$ cm, and the narrow Gaussian contained only 42.5% of the total area.

In order to interpret the results of our calibration procedures, it was also important to develop a model of the geometrical acceptance of our system. This depends not only on the detector geometry, but also on the energy and angular dependence of the calibration reaction and on multiple scattering of the detected particles. In the following subsection, we will review the data available on the $d + p$ elastic scattering cross section and the reasons for developing a common evaluation procedure for the $d + p$ data sets in our energy range.

D. Reference Cross Sections

A new evaluation has lowered the reference cross sections for $d+p$ elastic scattering used in our earlier publication [12]. The data and the new analysis leading to this conclusion will be presented in the following sections.

A luminosity calibration was run with an HD gas target before each of the $dd \to \alpha\pi^0$ production runs at 228.5 and 231.8 MeV. This means that we need to know the $d + p$ elastic scattering cross sections at $T_p = 114.3$ and 116.0 MeV, the equivalent laboratory proton beam energies. Bunker [47] has reviewed a number of early experiments [48–51] in addition to reporting their own measurements at 3 energies below 50 MeV. In particular, a widely spaced angular distribution is available at 93.6 MeV from Chamberlain and Stern [48]. Better data are reported at 146 MeV by Postma and Wilson [49] and at 155 MeV by Kuroda, Michalowicz, and Poulet [50]. Data at 65 MeV is available from measurements at RCNP [51]. From these data it is clear that the $d + p$ elastic cross section falls smoothly with increasing bombarding energy. More recently, cross sections have been reported by Sekiguchi at RIKEN using a polarized deuteron beam on a hydrogen target for $T_p = 70$ and 135 MeV [52]. As our CSB experiment was being completed, cross sections from a new

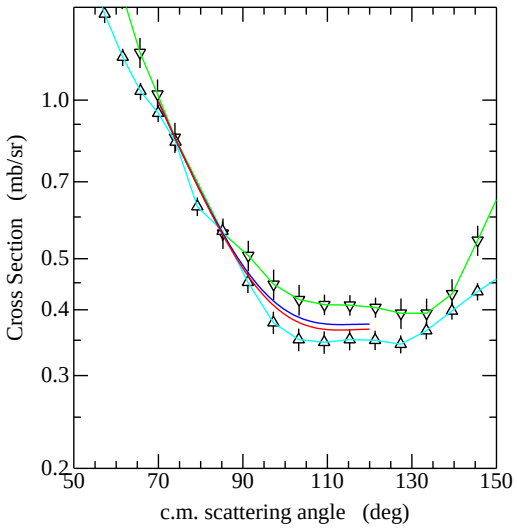

FIG. 8. Data for d+p elastic scattering from the KVI experiment [53] at 108 (down triangles with green connecting line) and 120 MeV (up triangles with blue connecting line). The blue and red curves represent the best fit at 114.3 and 116.0 MeV respectively.

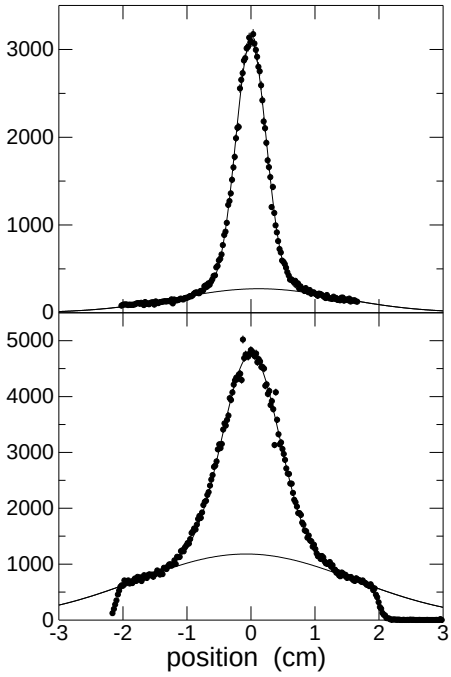

FIG. 7. The distributions of recoil deuterons from $d + d$ elastic scattering as a function of distance along the beam line in centimeters. The top panel is for production running and the lower panel is for the reduced pushing pressure used during the cross section calibration. The curves represent the background Gaussian and the sum of the foreground and background Gaussian shapes. The drop on the edges of the lower panel distribution mark the limits of the aperture in front of the position sensitive silicon detector.

experiment by Ermisch at the KVI provided data at 108, 120, 135, 150, 170, and 190 MeV [53].

An examination of these data reveals that within this energy range there are experimental inconsistencies in the data sets. Most notable is that at 135 MeV the data by Sakamoto [54] is about 20% smaller than that by Ermisch [53], while the newer Sekiguchi data [52] are about 30% smaller. The absolute normalization errors on the KVI measurements vary with energy between 5 and 6%, while the RIKEN data have even smaller errors. Thus, the $d + p$ data sets from these two labs are inconsistent. At the time of our original analysis of the CSB data, the data from the KVI seemed to join smoothly with the data at several other energies, including the measurements of Adelberger and Brown at 198 MeV [55] and Rohdjeß at 200 MeV [56]. In addition, the KVI data covered our energies of interest (114.3 and 116.0 MeV) with measurements at nearby energies (108 and 120 MeV). So, an interpolated set of values from the KVI experiment was used in the original $dd \to \alpha\pi^0$ analysis [12]. Some of the relevant angular distributions are shown in Fig. 8.

Subsequent to our CSB analysis, the group from Japan repeated the $d+p$ cross section measurements at 135 MeV

using multiple setups at both RIKEN and RCNP [57]. These new measurements fell close to the original results of Sakamoto and Sekiguchi, confirming that work. We have also obtained measurements at 100 MeV from RCNP prior to publication [60]. The cross section situation as a function of energy at $\theta_{c.m.} = 91°$ and $\theta_{c.m.} = 109°$ is shown in Fig. 9. Measurements as a function of energy close to these two center-of-mass angles are shown, and references are included in the figure caption. A dashed blue line is drawn through the KVI measurements to give a representation of the energy dependence of these data over this energy range. In all cases, the Japanese data are lower. If the energy dependence is taken as indicative of the cross section trend, but normalized instead to the Japanese data at these two angles, the solid blue lines result. These two angles were chosen because they brought together measurements from a wide range of experiments and because they fell near the center, and most important, region for the normalization of the CSB data. These Japanese measurements were checked in a number of independent ways [57] and appear to be more reliable. The solid blue line is a way to scale this reference to our energies of 114.3 and 116.0 MeV. We also chose to leave the angular shape of the curves in Fig. 8 unchanged. The renormalization coefficients are 0.940 at 91° and 0.854 at 109°. Our average renormalization is 0.90, which lowers the previous measurements [12] by this factor. It should be noted that the KVI and Japanese angular distributions are rather different [57] and that this region is one where the renormalization coefficient is relatively close to one. So the discrepancies between these two experiments involve more than a simple change of scale. Our interest here is in determining the $d + p$ elastic cross section within a limited range of angles and energies.

E. Final Luminosity Result

The various yields obtained in the cross calibration procedure are used to determine the factor needed to convert the luminosity monitor yield to an integrated luminosity. We may express N_{dd}^{HD}, the number of dd elastic scattering coincidences obtained using the HD target, as

$$N_{dd}^{HD} = \int \left(\frac{d\sigma}{d\Omega}\right)_{dd} f_{HD}(z)\varepsilon_{dd}(\theta,\phi,z)\ \mathcal{L}(t)\ dt\ dz\ d\Omega \tag{4}$$

where $\mathcal{L}(t) \equiv \frac{dN}{dt} \cdot n$ is the luminosity, $\frac{dN}{dt}$ is the number of beam particles per unit time, n is the number of target particles per unit area, $f(z)$ is the target density profile (with $\int f(z)dz = 1$), $\varepsilon(\theta,\phi,z)$ is the coincidence efficiency, and $\frac{d\sigma}{d\Omega}$ is the elastic scattering cross section. Note that $\int \mathcal{L}dt$, the integrated luminosity, factors out of the above integral.

A similar expression is obtained for each of the possible detector pairs for N_{dp}^{HD}, the number of dp elastic

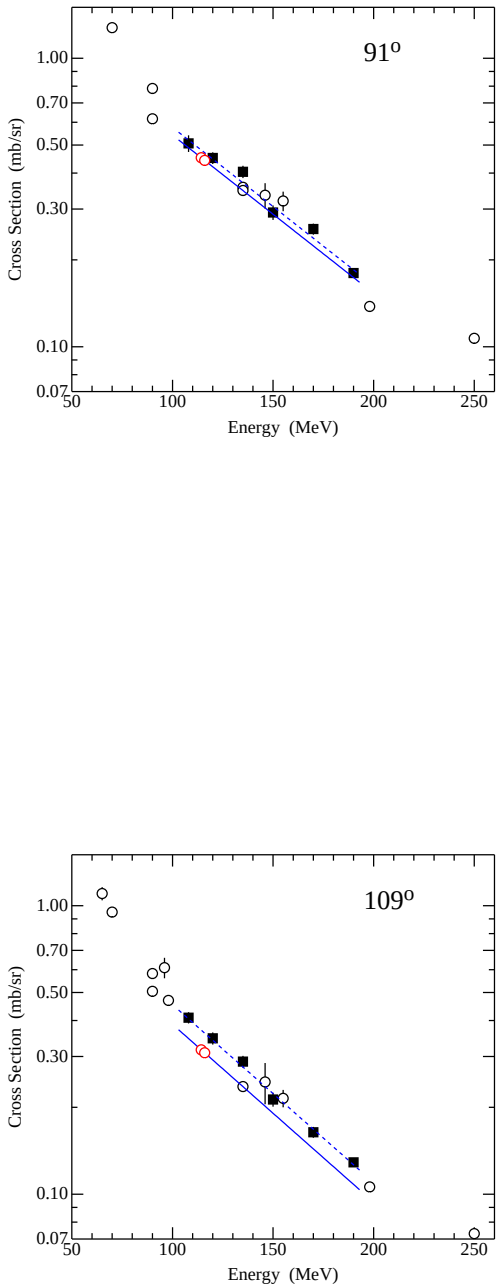

FIG. 9. Measurements of the center-of-mass cross section for $p + d$ elastic scattering in a narrow angle range and as a function of proton beam energy. The top panel shows data near 91° while the bottom panel shows data near 109°. The open circle data were measured at 65 [51], 70 [52], 90 [58, 59], 95 [48], 98 [60], 135 [52, 54], 146 [49], 155 [50], 198 [55], and 250 MeV [61]. The Ermisch data, represented by the solid squares, were measured at 108, 120, 135, 150, 170, and 190 MeV [53]. The dashed blue line represents a straight line on these graphs through the Ermisch data. The solid line intersects the Sekiguchi measurements at 135 MeV and has the same slope. The two red circles are located at 114.3 and 116.0 MeV along this line.

scattering coincidences obtained using the HD target.

$$N_{dp}^{HD} = \int \left(\frac{d\sigma}{d\Omega}\right)_{dp} f_{HD}(z)\varepsilon_{dp}(\theta,\phi,z)\ \mathcal{L}(t)\ dt\ dz\ d\Omega \tag{5}$$

In this expression the integrated luminosity again factors out of the integral. It is the same as the integrated luminosity for the dd yield because of the use of molecular HD target gas. As a result, the ratio of measured yields N_{dd}^{HD}/N_{dp}^{HD} is independent of the integrated luminosity.

1. Reaction Losses

The coincidence efficiency ε in the above two integrals can be factored into two terms: one which includes the geometrical acceptance of the detectors and the effects of multiple scattering; the other which describes the losses arising from nuclear reactions (in intervening materials before the detector and in the detector material itself) and our method of particle identification. The efficiency associated with the first term was calculated by creating a detailed model of the luminosity experiments using GEANT [62], with the effects from nuclear reactions disabled – since we wanted to have control over how those losses were evaluated. In order to evaluate the efficiency associated with the second term, we collected reaction cross section measurements for both protons and deuterons and we developed a simple model for the shape of the reaction tail in both ΔE and E detectors. For deuterons, the model is simplified by the fact that when they interact with a material, they almost always break up. For protons, the reaction tail is more complicated, but we used a model that assumed a simplified shape with either a flat tail or a triangular tail.

The losses arising from reactions were especially significant for the dp calibration events. The deuterons for these events went through a significant amount of material before being stopped in the ΔE-E detector stack at 25°. The coincident protons exiting at 44.2° went through less material, and were not stopped in the detectors. Calculations of losses arising from reactions and particle identification assumed a mean starting energy of 130 MeV for the deuterons and 98.5 MeV for the associated protons.

The 25° deuterons went through 1.09 g/cm^2 of steel in the target box, 3.22 g/cm^2 of aluminum in the exit window of the target box, and 0.37 g/cm^2 of plastic scintillator in the ΔE detector. These particles then entered the E detector where they were stopped. To include the effects of energy dependence of reaction cross sections, the E detector was broken into slabs each 10 MeV thick. The mean energy of the deuterons in each slab was calculated using range tables [63]. The mean energies for the deuterons in the material prior to the stopping detector were similarly computed.

The reaction cross sections for deuterons were obtained from four sources [64–67]. Auce *et al.* [64] provide reaction cross sections on targets from Be to Pb at 38, 65, and 97 MeV. Bäumer, *et al.*, [65] and Korff,*et al.*, [66] provide reaction cross sections at 170 MeV resulting from optical model fits to elastic and inelastic scattering data for many targets. We used ^{28}Si cross sections for Al, and ^{58}Ni cross sections for steel. Reaction cross sections for hydrogen were obtained from Carlson's compilation of cross sections for protons on targets ranging from deuterium through lead [67]. Carlson's compilation was also used for the reaction cross sections for protons exiting at 44.2°.

Measurements made by Lecollet *et al.* [68] of cross sections at small angles for ^{9}Be(d,n)X at 100 MeV indicate that half of the total reaction cross section measured by Auce *et al.* [64] can be attributed to (d,n)X. Since one expects the integrated cross section for (d,p)X to be the same, almost all the reaction cross section for deuterons at 100 MeV comes from its dissociation. Further evidence that very little of the deuteron reaction cross section can be attributed to inelastic scattering of the deuteron is given by Wu *et al.* [69], who measured cross sections for the charged particle spectra for 80 MeV deuterons on ^{27}Al and ^{58}Ni. If one takes the partial cross section for neutron emission to be the same as for proton emission, one finds that only 10% of the total reaction cross section can be attributed to inelastic scattering of the deuterons from ^{27}Al and only 5% for the case of deuterons from ^{58}Ni.

Our model indicates that 9.5% of the 25° deuterons experienced a reaction in the material before the E detector. Almost half of these were cases resulting in the escape of a fast neutron, so these were well outside the ΔE-E window used for deuteron PID. The other half were events yielding fast protons and almost all of these were lost because they were also well outside the deuteron PID window. Given our estimate that this model of the reaction cross section is good to about 10%, we end up with (9.5 ± 1.0)% of the deuterons lost in the material before the E detector.

Within the E detector, our model indicates that 13.6% of the 25° deuterons experienced a reaction before being reduced to an energy of 20 MeV. Deuterons experiencing a reaction with energies less than 20 MeV would be accommodated by the deuteron PID gate. As before, for the more energetic deuterons about half of the reactions will involve the production of a fast neutron and these events fall outside the PID gate, resulting in a loss of $13.6\%/2 = (6.8 \pm 0.7)\%$. For the events involving the production of a fast proton, only half of the energy of the deuteron will be collected from the proton. The associated neutron that interacted with a nucleus will give rise to other particles, some of which will deposit energy in the scintillator. One model for the resulting spectrum tail is that it is flat. Our PID window extends about a third of the way below the peak, resulting in a loss of $6.8\% \times 0.66 = 4.5\%$. Another possible model for the spectrum tail is one that falls linearly to zero. In this case we suffer a loss of $6.8\% \times 0.44 = 3.0\%$. Averaging the

results of these two models yields a loss of (3.8 ± 0.7)%. Thus, our final result for losses of the 25° deuterons in the E detector is (10.6 ± 1.0)%.

It is also possible for the 44.2° protons to experience reactions before entering the wedge luminosity detector system. These particles go through 1.40 g/cm^2 of steel in the target box, and 2.15 g/cm^2 of aluminum in the exit window of the target box. We calculate that 3.1% of these protons experience a reaction before the wedge detectors. Almost all of the reaction cross section for these 90 MeV protons comes from inelastic scattering. We consider two simple models for this energy distribution. In the first, the spectrum is flat in energy and the proton PID window extends half way below the peak. This gives rise to a loss of 3.1% × 0.5 = 1.6%. In the second, the spectrum is triangular in shape going to zero at 0 MeV. Using a PID window that extends half way below the peak, this yields a loss of 3.1% × 0.25 = 0.8%. Averaging the two models yields a loss of 44.2° protons of (1.2 ± 0.4)%.

Combining all of the losses due to reactions and PID for the *dp* calibration events, we obtain a net loss of (21.3 ± 1.5)%. Given the model uncertainties in these calculations, we quote a final value of (21 ± 2)% for losses in the yield N_{dp}^{HD} due to reactions and PID.

In a similar manner, we calculate losses for the $d+d$ luminosity monitor events that originate from reactions and particle identification. Here the PID correction is important because of the possibility of $d+p$ events creeping into the $d+d$ PID window. Because we ran three targets during the calibrations, (hydrogen (H_2), deuterium (D_2) and molecular HD) gas), we were able to develop a consistent model for these losses. The two deuterons exit at ± 44.2° about the target and pass through 1.40 g/cm^2 of steel and 2.15 g/cm^2 of aluminum before passing through the wedge detectors of the luminosity monitor. Losses due to reactions here are the same in the N_{dd}^{HD} yield as in the $N_{dd}^{D_2}$ yield, and cancel out in the final calculation of integrated luminosity (please see Eqn. 7 in Section IV.E.3).

2. *Angular dependence of* $\left(\frac{d\sigma}{d\Omega}\right)_{dd}$

In the two integrals appearing in Eqns. (4) and (5), everything is known except for $\left(\frac{d\sigma}{d\Omega}\right)_{dd}$. We assume this quantity to be slowly varying in the restricted angular region sampled by our luminosity monitor and we approximate it by a constant value at a center of mass angle of 90° which can be factored out of the integral. The remaining two integrals were then evaluated using Monte Carlo techniques and the simulation package GEANT [62].

There have been recent measurements of the differential cross section for *dd* elastic scattering with the BBS at the KVI at 180 MeV [58, 70]. These measurements show a minimum in the cm cross section at $\theta_{c.m.} = 90°$, that grows by less than 3% as one goes 5° away from the minimum, and by less than 13% as one goes 10° away from the minimum. The full angular acceptance of one of the luminosity monitor detectors is 6° in the lab or 12° in the cm. A Monte Carlo simulation of coincident $d+d$ events for the luminosity monitor system yields a FWHM of 8° in the cm, with 80% of the events in the region defined by this FWHM. We conclude that the effects of angular variation of the $d+d$ cross section on our luminosity monitor yields are much less than other systematic uncertainties associated with the monitor system.

3. *Calculated Integral Luminosity*

Our calculations of the integrated luminosity did not depend explicitly on an extracted cross section for $\left(\frac{d\sigma}{d\Omega}\right)_{dd}$. Using terminology similar to what was used in Eqns. (4) and (5) we may write down an expression for the integrated luminosity observed in CSB production running with a D_2 gas jet target as:

$$\int \mathcal{L}dt = \frac{N_{dd}^{D_2}}{\left(\frac{d\sigma}{d\Omega}\right)_{dd} \int f_{D_2}(z)\varepsilon_{dd}(\theta,\phi,z)\, dz\, d\Omega} \qquad (6)$$

where $N_{dd}^{D_2}$ is the number of $d+d$ elastic scattering coincidences obtained using the D_2 gas jet target. The integral in the denominator was evaluated using Monte Carlo techniques and the GEANT [62] package in the same manner as the integrals evaluated for the cross calibration procedure.

The ratio of Eqn. (5) to Eqn. (4) yields a result for $\left(\frac{d\sigma}{d\Omega}\right)_{dd}$ that can be substituted into Eqn. (6) to obtain our working formula for calculating the integrated luminosity:

$$\int \mathcal{L}dt = N_{dd}^{D_2}(N_{dp}^{HD}/N_{dd}^{HD})(I_{dd}^{HD}/I_{dd}^{D_2})(1/S_{dp}^{HD}) \qquad (7)$$

with the following two integrals for the acceptance and coincidence efficiency of the $d+d$ detector system

$$I_{dd}^{HD} = \int f_{HD}(z)\varepsilon_{dd}(\theta,\phi,z)\, dz\, d\Omega \qquad (8)$$

and

$$I_{dd}^{D_2} = \int f_{D_2}(z)\varepsilon_{dd}(\theta,\phi,z)\, dz\, d\Omega \qquad (9)$$

and a new integral that is a cross section weighted acceptance and coincidence efficiency for the *dp* system

$$S_{dp}^{HD} = \int \left(\frac{d\sigma}{d\Omega}\right)_{dp} f_{HD}(z)\varepsilon_{dp}(\theta,\phi,z)\, dz\, d\Omega \qquad (10)$$

Equation (7) shows that explicit knowledge of the $d+d$ elastic cross section $\left(\frac{d\sigma}{d\Omega}\right)_{dd}$ is not needed for our determination of the integrated luminosity. It also shows that systematic uncertainties arising from the luminosity monitor are in large part eliminated by cancellation

resulting from taking the ratio $I_{dd}^{HD}/I_{dd}^{D_2}$. The only significant difference between elements of the two integrals comes from the different target density profiles, $f_{HD}(z)$ and $f_{D_2}(z)$. These profiles were determined with good precision during both the calibration and the production runs, as illustrated in Fig. 7 and discussed in Section IV.C. The spatial region along the beam sampled by the luminosity monitor is centered on the gas jet position, and has a full width of 4.0 cm . This region is well within the region sampled by the profile monitor, which extends sufficiently beyond the peak to provide a good determination of the "tails" of the target profile.

The primary source of systematic uncertainty in the end result for the integrated luminosity comes from evaluation of the term S_{dp}^{HD}, the integral associated with the $d+p$ events from the cross calibration. This includes a 5% uncertainty in the $d+p$ elastic cross section and a 7% uncertainty in the acceptance and efficiency of the detectors used in the cross calibration.

F. Summary

Our extensive and detailed study of the luminosity calibrations yielded three major effects on our final integrated luminosities that were not known at the time of our initial publication of results [12].

The first of these is an improved determination of the cross sections $\left(\frac{d\sigma}{d\Omega}\right)_{dp}$. The new value is about 10% smaller than what was used in the earlier calculations. As seen in Eqns. 7 and 10, this results in a 10% increase in the computed integrated luminosity.

The second comes from including reaction losses in the calculation of the corrected yields for N_{dp}^{HD}. As seen in Eqn. 7, this results in a 21% increase in the computed integrated luminosity.

The third effect comes from an improved computational model of the luminosity system and its calibration. Using GEANT and Monte Carlo methods a more accurate simulation of the apparatus involved was constructed. The results of the calculations yielded values for the integral luminosities that were about 18% smaller than those calculated earlier [12].

These three effects together result in a net increase in the computed integral luminosity that is 13% larger than was originally thought.

V. DATA ANALYSIS

In this section we describe the analysis of the primary CSB measurements. Raw information in the form of signal sources had to be collected, processed, and event-by-event recorded. Multiple event streams (see Sec. II.F) allowed us to record several types of events simultaneously. Since the analysis of this experiment would require that the events be replayed offline many times, as much as possible of the critical information from the Pb-glass gamma detectors surrounding the gas jet target and the wire chambers and scintillator detectors in the magnetic channel needed to be retained. A number of procedures are described that had to be carried out in order to obtain cross sections for the $dd \to \alpha\pi^0$, $dd \to \alpha\gamma\gamma$, and $dd \to \alpha\pi^0\gamma$ reactions at each energy.

A. Software Corrections to the Raw Data

One of the challenges of this experiment involved operating the detectors over a period of several months in the environment of an intense deuteron beam circulating in the Cooler storage ring. Although the beam losses in the ring were small, they still produced intense neutron and proton backgrounds for many of the detectors. Both high count rates and temperature variations meant that it was important to monitor both pulse height gains and DC offsets of many of the detectors. These effects also resulted in small changes in measured times that had to be carefully tracked over the course of the production runs.

The CSB γ's had energies between 46 MeV and 106 MeV. For the Pb-glass detectors, both the pulse height (ADC) and the time (TDC) information were crucial. Because the online gamma ray histograms contained only the pulse height data from the module with the highest pulse height, these spectra were incomplete. The cosmic ray muon event stream was developed as a more suitable way to monitor the pulse heights and DC offsets of all of the detectors. During production running the Pb-glass phototube gains were updated daily using this procedure.

The CSB ^{4}He recoils originating at the target in a narrow forward cone had energies between 106 MeV and 121 MeV. Wire chambers and plastic scintillators in the magnetic channel were used for event triggering, particle identification and measurement of the four-momentum of each ^{4}He recoil. The proton rate into the magnetic channel from deuteron breakup was about 10^5 s^{-1}. Count rates in the channel detectors were substantially reduced by vetoing the longer range protons, reducing wire chamber high voltage to keep proton tracks below threshold, setting time-of-flight (TOF) windows to miss most protons, making $\Delta E1$ so thin that we could use a lower level discriminator to eliminate many of the protons, and dividing $\Delta E1$ into four quadrants. Since both the pulse height (ADC) and the time (TDC) information were again crucial, the ADC gains, DC offsets, and TDC time offsets for these scintillators were examined on a run-by-run basis. No changes in gain due to high rate were seen in any of the four quadrants making up the ΔE1 detector.

B. Identification of $dd \to \alpha\pi^0$ Events

The crucial feature of this experiment is its ability to distinguish the CSB $dd \to \alpha\pi^0$ reaction from the isospin-

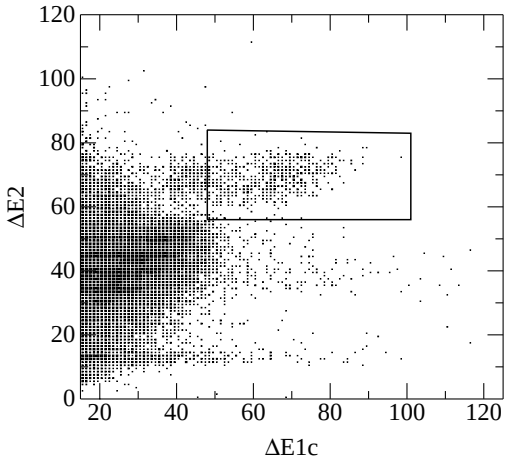

FIG. 10. Scatterplot of the energy deposited in the ΔE2 detector versus one quadrant of the ΔE1 detector. The scales represent ADC channel numbers. The zero is suppressed in order to avoid a large peak in the lower-left corner from protons. The He band appears above and to the right of the proton pileup events. The window is drawn around the ^{4}He portion so that losses may be avoided. A clean separation from ^{3}He is not possible in this spectrum alone.

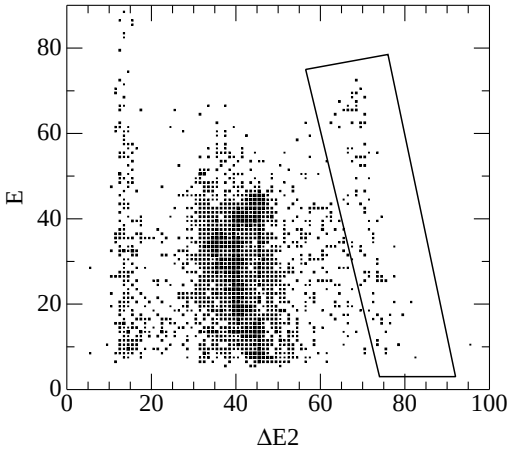

FIG. 11. Scatterplot of energy deposited in the E detector versus the ΔE2 detector. The window is drawn around the ^{4}He group. This feature contains a continuum of ^{4}He generated from (d,^{4}He) reactions on residual gas and pumping baffles in the main scattering chamber. Events from $dd \rightarrow \alpha\pi^0$ reactions are found in the upper part of this band.

allowed double radiative capture $dd \rightarrow \alpha\gamma\gamma$ reaction. First, we consider the particle identification (PID) of ^{4}He nuclei by their energy loss in the three plastic scintillators: ΔE1, ΔE2, and E. The ^{4}He PID is illustrated in Fig. 10, which shows a histogram of ΔE2 versus a quandrant of ΔE1 pulse heights, and Fig. 11, which shows a histogram of E versus ΔE2 pulse heights, for events passed by the magnetic channel in the CSB production run at 228.5 MeV. In these two scatterplots, the gate in Fig. 10 applies to the events shown in Fig. 11. The locus around the ^{4}He group in Fig. 11 indicates how these histograms cleanly identify the ^{4}He flux. Unfortunately, the rate of this flux is too high by about a factor of 10^3 for these ^{4}He's to have originated in $dd \rightarrow \alpha\pi^0$ or $dd \rightarrow \alpha\gamma\gamma$ reactions. There is apparently a ^{4}He flux without coincident gammas which may have originated from (d,^{4}He) reactions on residual gas and storage ring apertures. They are broadly distributed in energy and angle and we hypothesize that their spectrum represents an overlap of phase space and the acceptance of the coupled Cooler and magnetic channel. This feature in Fig. 11 thus shows events down to the electronic threshold on the energy scintillator.

Next, we consider the effect of adding the detection of one or two high energy gamma rays in coincidence to the ^{4}He event conditions. Our CSB event stream added the condition to the magnetic channel event that at least one Pb-glass Cerenkov detector fired in coincidence. This enabled us to look for these events in the online spectra. As production running continued, we initiated an offline replay analysis so that we could mount a more sophisticated search for the CSB events that might come in at a rate of one per day. As described in Sec. III.C, cluster summed pulse heights were constructed for the Pb-glass arrays to the left (γ_{Left}) and to the right (γ_{Right}) of the beam. This increased the gamma pulse height and greatly improved the signal-to-noise ratio in these spectra.

Figure 12 shows a histogram of γ_{right} TOF versus γ_{right} pulse height for events passed by the magnetic channel with a window on the ^{4}He recoils (left side panel).

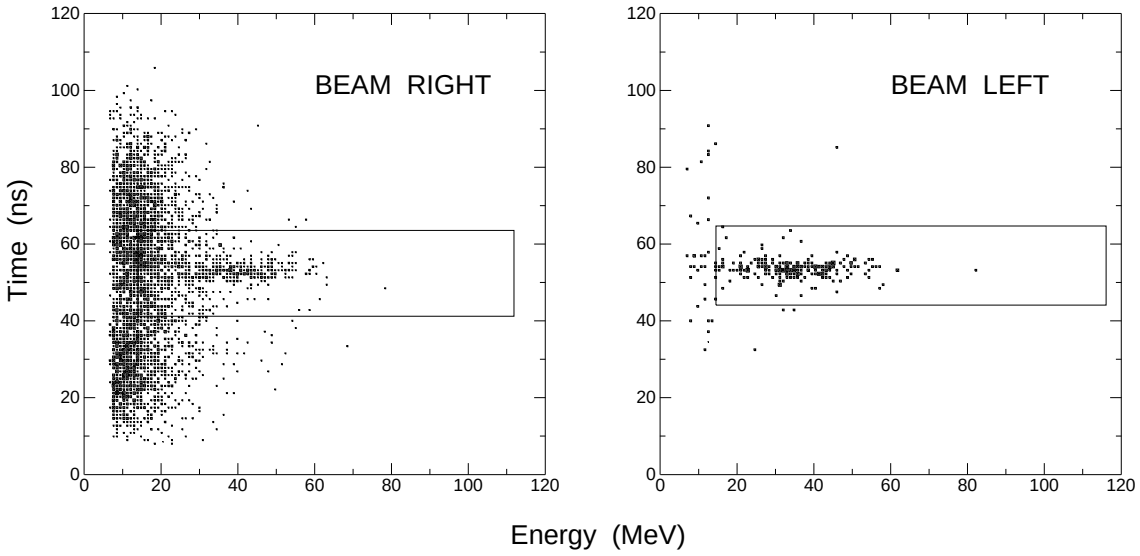

FIG. 12. Scatterplots of the beam right and left Pb-glass array showing the time of the largest Pb-glass event relative to the trigger timing of ^{4}He events in the magnetic channel. All such pairings are shown for beam right. In that spectrum, a rectangular window selects events that are in coincidence with the magnetic channel and above roughly 15 MeV (similar to the window for beam left). A similar display is shown for beam left, but for *only* those events that fall within the window for beam right. This eliminates much of the random background at low pulse height. The gate on good π^0 decays is very clean.

The locus for ^{4}He-γ coincidences is clear, but merges with the random coincidences at low pulse height. The rectangular box shows where we expect good ^{4}He-γ events to appear. If events in this box are further sorted based on beam left TOF and pulse height, then most of the random background is eliminated (right side panel). A similar rectangular box selects the events of interest.

Finally, as discussed in Sec. II.A and Sec. III.C, we determined the missing mass (MM) for each of the ^{4}He recoils determined to be in coincidence with two high energy gamma rays. The MM is computed using conservation of energy and momentum, the beam energy determined from the measured Cooler circumference and the Cooler RF frequency, and the vector momentum and energy of the ^{4}He recoil as obtained from the magnetic channel. The z-component of the momentum of each recoil was measured using time of flight between the first scintillator (ΔE1) at the exit of the septum magnet and the second scintillator (ΔE2) at the end of the channel about 6 m downstream. The transverse momentum component of each recoil was calculated from a measurement of its scattering angle in the wire chamber (WC1) located in front of the septum magnet. When this procedure was carried out with the calibration reaction $pd \to h\pi^0$, the result (recall Fig. 5) was a ^{3}He recoil MM spectrum with a π^0 peak whose FWHM was 240 keV for a run that lasted several hours.

Initially, for the $dd \to \alpha$X reaction, the ^{4}He recoil MM spectrum was so washed out that there was only just a hint of the π^0 peak near the endpoint of the spectrum. In this case the time it took to accumulate the spectrum was several days. Since maintaining time stability in the ΔE1-ΔE2 TOF spectrum at the level of 0.2 ns is required for the best MM resolution, we examined all of those experimental factors that might lead to a degradation of this resolution. These included: sensitivity of photomultiplier tube (PMT) gains to temperature variations in the Cooler vault where the temperature was not regulated; jumps in timing that occur when experimenters adjust the PMT high voltages or swap out related equipment that fails; PMT signal transit time drifts and occasionally jumps as the tube ages in response to heat; changes in other parts of the missing mass reconstruction process such as the dispersions of the 6° bending magnet and the dipole septum magnet; and changes in the beam tune of the Cooler.

To make run-by-run corrections to the ΔE1-ΔE2 TOF, we needed a marker from among the more numerous charge one particles traversing the magnetic channel. We selected a spatially localized group of low energy deuterons that stopped at the back of the E scintillator. We were able to track the positions of this bundle of rays using positions in all three wire chambers (WC1, WC2 and WC3), and then examined the TOF peaks for each of the four ΔE1 quadrants. By introducing a separate time offset for each quadrant, we discovered that we could improve the MM resolution by adjusting the four ΔE1 time offsets. Our production running started at a deuteron energy of 228.5 MeV, an energy chosen because the 1.21° recoil cone was expected to fit well inside the channel acceptance. As a result of these timing offset issues, we were unable to evaluate our data until close

to the end of the first production run when there were enough $dd \to \alpha\pi^0$ events available to check and improve the choices of these time offsets.

At that point the missing mass resolution was still poor, the separation between $dd \to \alpha\pi^0$ and $dd \to \alpha\gamma\gamma$ events was not crisp as it had been for $pd \to h\pi^0$, and the width of the π^0 peak meant that the peak was not well separated from the ^{4}He + γ + γ kinematic upper limit of 136.4 MeV. The decision was made to complete production running at the higher energy of 231.8 MeV, corresponding to a 1.75° recoil cone that extends a bit outside the channel acceptance and a kinematic end point of 138.0 MeV. Although we would lose an additional 18% of the π^0 events in the channel, we expected there would be a clear distribution of double radiative capture events on either side of the π^0 peak. Continuing the offline analysis, we eventually used the fact that for the $dd \to \alpha\pi^0$ events the MM should be independent of the ΔE1-ΔE2 TOF to determine sets of the four time offsets for each run that would give the best FWHM of the π^0 peak.

In our final offline analysis for this publication, we were able to include a number of effects that improved the final resolution of the π^0 peak by about a factor of two. The most important effect to include involved the long-term time stability of our recoil TOF measurement. It was also important to track the energy lost in all of the materials in the upstream part of the magnetic channel in order to obtain the correct recoil momentum for event-by-event reconstruction of the missing mass. The cluster summed gamma spectra also benefited from having a uniform cosmic ray peak for every Pb-glass block. Taking all these effects into account, the best missing mass resolution we could obtain for the several week period of each production run was 510 keV at 228.5 MeV and 660 keV at 231.8 MeV. This was sufficient to make a separation of the ^{4}He recoil spectrum into $dd \to \alpha\pi^0$ and $dd \to \alpha\gamma\gamma$ events. This separation and the determination of the two cross sections will be described in Sec. V.D.

C. Efficiency and Acceptance Factors

Several efficiency and acceptance factors had to be applied to convert the CSB yields into cross sections for $dd \to \alpha\pi^0$. The uncertainties in these factors were minimized by a detection apparatus that provided high efficiency and large acceptance. There were three inefficiency corrections (MWPC inefficiency; scintillator inefficiency; and reaction losses), each of small size, that could be determined with good precision and accuracy via straightforward means. However, the efficiency for π^0 detection and the acceptance of the magnetic channel required more computational effort.

In parallel with our data analysis, we built a detailed simulation of the experiment using software available with the GEANT package [62]. This simulation provided the means to determine the small corrections (totaling less than 10%) to our *measured* π^0 detection efficiency for $pd \to h\pi^0$ to obtain the necessary π^0 detection efficiencies for $dd \to \alpha\pi^0$ at two energies. This simulation package also provided the means to compute the reductions to the acceptance of the magnetic channel due to detector sizes, obstructions in the channel and multiple scattering.

1. π^0 detection efficiency

The largest numerical corrections to the extracted CSB yields come from the efficiency for π^0 detection. By making measurements close to threshold, where the speeds of the π^0's were small and the opening angles for their two decay γ's were large, most of the efficiency corrections arose from the geometric acceptance of the Pb-glass detector arrays. The detailed Monte Carlo simulation of the experiment in which the efficiency for π^0 detection in $pd \to h\pi^0$ was calculated (see Sect. III.C.) gave an efficiency that differed from the measured result by only 0.0041 (1.2%). This is excellent agreement and the difference is well within our estimates of the systematic uncertainties in the measurements.

TABLE II. Comparison of kinematic factors leading to differences in π^0 detection efficiency for the three cases in the text. Final detection efficiencies include all corrections in the text.

Reaction	$pd \to h\pi^0$	$dd \to \alpha\pi^0$	$dd \to \alpha\pi^0$
beam particle	p	d	d
beam energy (MeV)	199.4	228.5	231.5
cm cross section	forw. peaked	isotropic	isotropic
$\sigma(0°)/\sigma(180°)$ (cm)	1.9	1	1
^{3}He cone angle	0.95°	1.21°	1.75°
π^0 cone angle	20.3°	35.4°	57.3°
π^0 lab energies (MeV)	1.2 - 5.9	0.7 - 10.2	0.1 - 14.1
γ lab energies (MeV)	50 - 90	46 - 98	44 - 106
min $\gamma - \gamma$ lab angle	146.8°	136.6°	129.6°
calc π^0 det eff	0.3567	0.3391	0.3206
meas π^0 det eff	0.3526	na	na

Almost all of the differences in π^0 detection efficiency for the CSB measurements from each other and from the $pd \to h\pi^0$ calibration measurements arise from kinematic effects. These effects are summarized in Table II. The π^0 cone for the $pd \to h\pi^0$ calibration measurements was 20.3°. For the CSB measurements at 228.5 MeV this cone increased to 35.4°; and for the CSB measurements at 231.5 MeV it increased further to 57.3°. As cone size for the π^0's increases, more and more of the correlated $\gamma - \gamma$ pairs are pushed out of the acceptance of the two, semi-planar detector arrays about the target, giving rise to increasing inefficiency. This geometric effect is further increased by a decrease in the size of the minimum opening angle between correlated $\gamma - \gamma$ pairs: this angle is 146.8° for the $pd \to h\pi^0$ calibration measurements, drops to 136.6° for the CSB measurements at 228.5 MeV, and drops further to 129.6° for the CSB measurements

at 231.5 MeV.

Kinematics also give rise to significantly different π^0 energies for the three reactions, which in turn gives rise to a decrease in the minimum γ energy for each of the three reactions (see Table II). Although the lower level sorting cut was below these energies (effectively 27 MeV for the left array, and 25 MeV for the right array), the poor resolution of the Pb-glass modules (50% for the left array and 40% for the right array for 70 MeV γ's) gave rise to small tails extending below this threshold cut. As a result, kinematic effects driving the minimum γ energy closer towards the threshold cut will contribute to increasing the inefficiency for π^0 detection.

The efficiencies for the three reactions studied are also influenced by the angular distribution of the π^0's. The angular distribution for the π^0's in the center of mass for $pd \rightarrow h\pi^0$ was extracted from the systematics of published measurements [42]. This angular distribution was significantly forward peaked and had the Legendre expansion:

$$(75.4 \text{ nb/sr})P_0 + (24.4 \text{ nb/sr})P_1 + (1.7 \text{ nb/sr})P_2 \ .$$

One obtains a $\sigma(0^\circ)/\sigma(180^\circ)$ ratio of 1.9 for this cross section in the center of mass (cm). The forward peaking arises because of the large $s-p$ wave interference for the reaction [42]. For the CSB reaction $dd \rightarrow \alpha\pi^0$ this interference is not possible, and the cross section in our energy range is expected to be very close to isotropic.

The efficiencies calculated for π^0 detection in the CSB measurements were 0.3391 $\pm$ 0.0009 (stat) $\pm$ 0.0034 (sys) at the lower beam energy (228.5 MeV), and 0.3206 $\pm$ 0.0009 (stat) $\pm$ 0.0032 (sys) at the higher beam energy (231.8 MeV). These efficiencies incorporate corrections for dead Pb-glass modules, for losses due to the width of the gates in the gamma times, and for losses due to corruption of the gamma times for the multiplexed tdc signals. The quoted systematic errors arise primarily from uncertainties in the last two corrections.

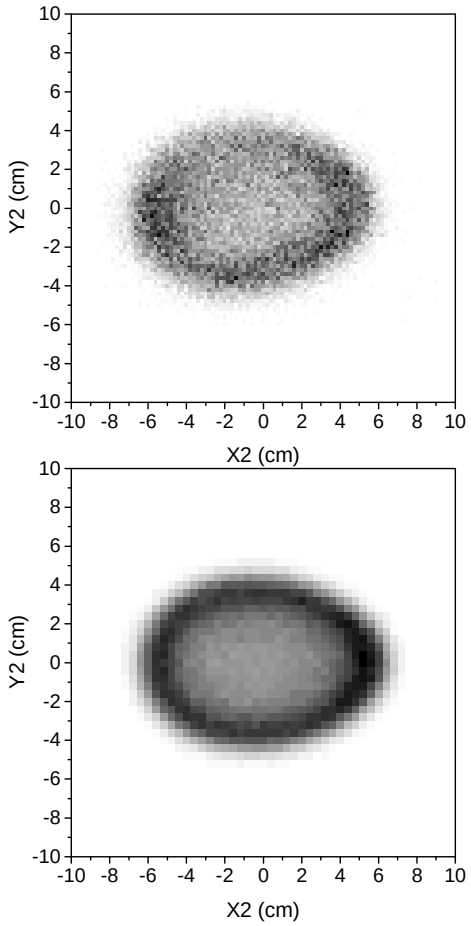

FIG. 13. (top) The locus of ^{3}He recoils observed in WC2 for the $pd \rightarrow h\pi^0$ calibration run made at a proton beam energy of 200.2 MeV. (bottom) The locus of events obtained for the simulation.

2. *Channel acceptance*

The losses in the magnetic channel were kept small by running close to threshold, using magnetic elements with relatively large gaps, and placing focusing elements at key points along the channel. Data for the resulting trajectories of the ^{3}He recoils in the $pd \rightarrow h\pi^0$ calibration run were obtained from the three wire chambers in the channel: WC1 located at the entrance of the septum magnet; WC2 located at the exit of the septum magnet and in front of the first quadrupole (Q1); and WC3 located at the exit of the channel pipe.

These data were used to test the simulation model developed for the apparatus, which also used the GEANT package [62]. Field maps of the magnetic elements were incorporated into the model. These maps included the fringe fields of each magnetic element, which was important for these large-gap magnets. Physical obstructions in the channel were incorporated into the model, along with all the materials through which the recoils passed.

The small amount of vertical focusing observed in WC1 (see Fig. 4) is easily reproduced by the simulation. The stronger focusing effects of the septum magnet provide a much better test of the model. At the top in Fig. 13 we see the locus of ^{3}He events in WC2 obtained from a calibration run at 200.2 MeV, and at the bottom in Fig. 13 we see the locus of events obtained from the model. The agreement is very good. Also, at WC2 one begins to notice the effects of multiple scattering, but they are seen to be small.

At this time, we also examined the X- and Y- projections of the ^{3}He recoils from the calibration run in WC3 at the exit of the channel pipe. In comparing our WC3

measurements with our calculated distributions, these results illustrate how well the channel simulation models the focusing effects of the three quadrupoles, and also how well it models the multiple scattering of the recoils. Multiple scattering is far more evident in WC3 because of the nearly 3 meter long flight path in the channel pipe.

The fields used in the CSB calculations were scaled according to the measured currents in the magnetic elements. In Table III are shown the computed fraction of CSB recoil ^{4}He's surviving at various key locations in the channel for each of the two beam energies. The fraction surviving at E, the stopping scintillator, is the *acceptance* of the magnetic channel.

TABLE III. Calculated transmission of CSB recoils at key locations in the magnetic channel at 228.5 MeV (cone angle = 1.21°) and at 231.8 MeV (cone angle = 1.75°). The statistical uncertainty for each of the tabulated values is ±0.001.

Location	Trans at 228.5 MeV	Trans at 231.8 MeV
6° mag exit	1.000	1.000
WC1	1.000	0.916
WC2	0.999	0.909
Δ E1	0.999	0.908
Q1 exit	0.998	0.897
Q2 exit	0.995	0.875
Q3 exit	0.992	0.861
Pipe center	0.989	0.852
WC3	0.984	0.844
E	0.971	0.794

At the lower beam energy (228.5 MeV), our model yields very small losses in the channel. At this energy the cone of recoil ^{4}He's (1.21°) is well contained by the channel and we obtain a channel acceptance of 0.971 ± 0.001(statistical).

At the higher beam energy (231.8 MeV), the losses in the channel are larger. As a result of the increased size of the recoil cone (1.75°), more of the multiply scattered recoil ^{4}He's hit various obstructions in the channel and more lie outside the sensitive regions of the detectors. A majority of these losses occur at WC1, because a piece of the recoil cone closest to the beam falls outside of the sensitive region of WC1, resulting in a loss of about 8.4%. Further losses occur along the channel (see Table III) as multiple scattering and the large size of the cone pushes ^{4}He's out of the channel and its detectors. We see a second loss of significance at the very end of the channel, in the E detector. Our running with this large sized cone was not anticipated in the design of the experiment, and the vertical size of E was insufficient to contain the recoils coming out of the end of the channel. This resulted in an additional loss of about 4.9%. We obtain a final channel acceptance of 0.794 ± 0.001(statistical) for the data obtained at 231.8 MeV.

3. MWPC inefficiency

The efficiencies for the individual wire chamber planes were measured continuously throughout the experiment. Event type (1), magnetic channel events, were used for this purpose (see Sec. II.F.). These were events in which ΔE1, ΔE2, and E fired in coincidence, and neither veto scintillator fired. The coincidence timing was set to include mass 3 and 4 particles, so as to avoid the bulk of the faster protons in the channel. A window was placed on ^{4}He's spanning the range of energies of the CSB recoils. Each of the scintillation detectors was made small enough relative to the closest wire chamber to ensure that these particles had to go through the sensitive region of each wire chamber. Due to its high rate, WC1 was constructed of three planes (x, y and u) to allow for recovery of some classes of multiple hits. WC2 and WC3, located after the septum magnet, had lower rates and were constructed of only two planes (x and y). To further reduce the number of hits, each of the wire chambers was optimized for the detection of charge two particles.

WC1, located at the entrance to the septum magnet, had the highest rate and there were a number of multiple hits. Since the position of the recoil particle at WC1 was used to determine its transverse momentum, an effort was made to "rescue" some of those multiple hit events. Listed in Table IV are the categories of hit patterns dealt with for WC1, and the action taken for each case. Hit patterns not listed were discarded.

TABLE IV. Actions taken for various hit patterns in WC1.

No. x-hits	No. y-hits	No. u-hits	Action
1	1	1	take (x, y)
1	1	0	take (x, y)
0	1	1	take y, calculate x
1	0	1	take x, calculate y
1	1	2	take (x, y)
1	2	1	best fit (x, y)
2	1	1	best fit (x, y)
1	2	2	best fit (x, y)
2	1	2	best fit (x, y)
2	2	1	best fit (x, y)

WC2 (located between the septum magnet exit and Q1) and WC3 (located at the end of the magnetic channel) had substantially less rate than WC1. As a result there were fewer multiple hits in these wire chambers. For these wire chambers we accepted as a valid hit only those that triggered one wire, or two adjacent wires, in a given plane. Hits in WC2 and WC3 were not required in the sorting of CSB events. Position information from these chambers was used for diagnostic purposes only.

A shift (8 hours) of running provided sufficient events to determine the efficiency of each wire chamber to a statistical precision of better than ±0.01. The total efficiency for WC1 averaged to 0.93 for the runs at 228.5 MeV, and averaged to 0.95 for the runs at

231.8 MeV. The efficiencies for the other two wire chambers were higher.

4. Trigger inefficiency

The large flux of protons through the magnetic channel, arising from deuteron breakup at the target, motivated the implementation of the double veto arrangement. With it, the efficiency for vetoing protons exceeded 99.99% at all times, and served effectively to reduce the rate being recorded event-by-event.

Since the large flux of protons through the magnetic channel gave rise to large rates in each of the two veto detectors, it resulted in *accidental* vetoes. To correct for this, separate circuits were set up in parallel with the circuit for event type (1) (see Sec. II.F.). In each of these parallel circuits, one of the veto detectors was delayed and then put into coincidence with a trigger consisting of a valid coincidence between ΔE1, ΔE2, and E, with a requirement of no prompt signal from the other (undelayed) veto. The delay was sufficiently long that this provided a direct measure of the accidental vetos from the delayed veto detector. Another identical circuit was set up to make the same measurement for the other veto detector.

The signals for these parallel circuits went into scalers and provided sufficient rate to continuously monitor the fraction of events lost because of accidental vetoes to a statistical precision better than 0.1% each hour. The fractions measured scaled directly with the rates in the veto detectors, as expected. Trigger efficiencies corrected for these losses were typically 0.94 for the measurements at 228.5 MeV, and 0.96 for the measurements at 231.8 MeV.

Additional trigger losses were generated by the system livetime of the CAMAC acquisition system and the computer with which it was interfaced. These losses were monitored continuously by scaling our triggers into the system and also by scaling the triggers accepted by the system for processing. The rates were sufficient to determine these losses to a statistical precision better than 0.1% each hour. The measured system livetime was typically 0.95 for the measurements at 228.5 MeV, and 0.94 for the measurements at 231.8 MeV.

5. Reaction losses

CSB ^{4}He nuclei originating at the target had energies uniformly distributed from 107 MeV to 117 MeV for the 1.21° cone at 228.5 MeV and from 106 MeV to 121 MeV for the 1.75° cone at 231.8 MeV. These recoils passed through a number of windows, wire chambers, air gaps, plastic scintillator material, and detector wrapping materials as they moved through the magnetic channel. In the course of this travel some fraction of the ^{4}He nuclei were lost because of nuclear reactions. For the channel it was important to include all of these materials, no matter how thin. The fraction of the ^{4}He nuclei lost was calculated using information available in the literature [71, 72] on total reaction cross sections for ^{4}He on the above materials for energies near 100 MeV. Auce *et al.* [71] obtained total reaction cross sections for 75-190 MeV ^{4}He on targets from ^{12}C to ^{208}Pb. Igo and Williams [72] obtained total reaction cross sections for 40 MeV ^{4}He on targets from ^{9}Be to ^{232}Th. The calculations we performed took into account the variation in energy of the ^{4}He nuclei as they traversed the channel, as well as the variation with energy of the reaction cross sections as deduced from the above references. Because the band of ^{4}He energies was narrow for each of the CSB runs, we assumed a starting energy of 112 MeV, corresponding closely to the mean ^{4}He energy in each case.

In order to account for corrections arising from reaction products falling within the windows used in the sorting of CSB events, continuum spectra for alpha-induced reactions were examined [73, 74]. Bertrand and Peelle [73] obtained spectra for charged particle emission for 58 MeV ^{4}He nuclei incident on a number of targets. Wu, Chang, and Holmgren [74] obtained spectra for charged particle emission for 140 MeV ^{4}He nuclei incident on a number of targets. These papers show that only a tiny fraction of the reaction cross section is near the elastic peak - almost all of it is highly inelastic. From these works we deduce that less than 2% of the reaction cross section is within 20% of the energy of the elastic peak. Hence, we assume in our calculations that any ^{4}He undergoing a reaction will generate signals outside of our sorting gates and is lost.

The calculations yielded a loss of 0.42% in the ΔE1, of 1.29% in the ΔE2, and of 0.61% in the E detector. Adding in the losses generated in the other materials in the channel, we obtain an overall loss of 3.05% from reactions. This results in a correction to our CSB yields of 0.970 ± 0.005 (systematic), where the quoted systematic uncertainty arises from uncertainties in our extrapolations of reaction cross sections to the energies relevant here.

D. Cross Section Analysis

The resulting Missing Mass (MM) spectra obtained for the two bombarding energies are shown in Fig. 14. Careful study of the data indicate that less than 1% of the observed counts can be attributed to accidentals, or other nonphysical processes. We find a narrow peak coming from CSB ($dd \rightarrow \alpha\pi^0$) sitting on a continuum dominated by double radiative capture ($dd \rightarrow \alpha\gamma\gamma$). The maximum MM allowed by kinematics is 136.4 MeV at the lower bombarding energy (228.5 MeV), very close to the CSB peak at the π^0 mass of 134.98 MeV/c^2. At the higher bombarding energy (231.8 MeV) the kinematic end point of the continuum is at 138.0 MeV/c^2, and better separated from the CSB peak.

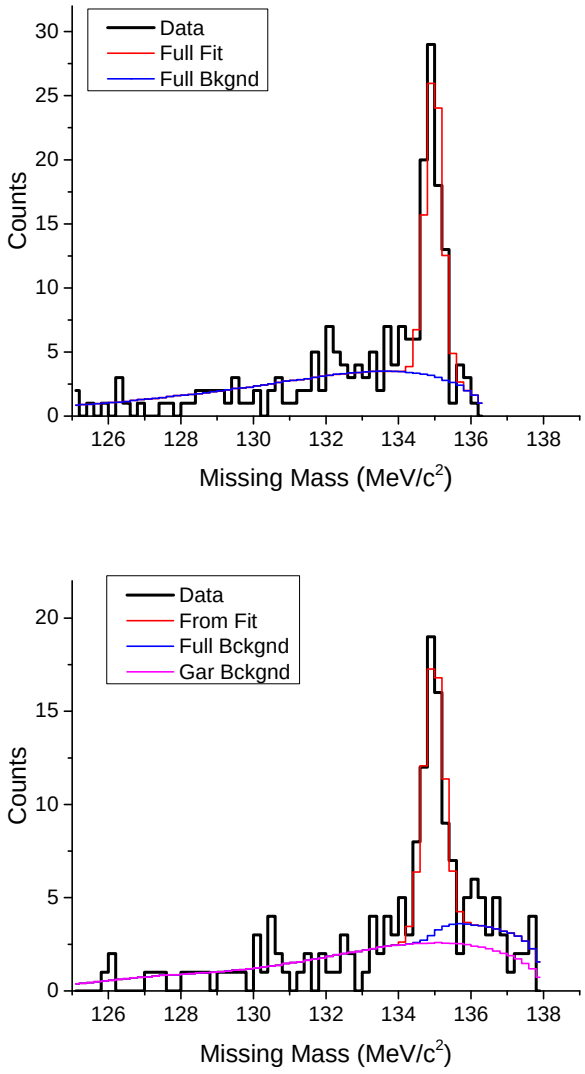

FIG. 14. Candidate $dd \rightarrow \alpha\pi^0$ events at 228.5 MeV (top) and 231.8 MeV (bottom) as a function of missing mass. The solid black spectrum shows both a narrow peak at the π^0 energy and a more broadly distributed background of mostly double radiative capture. The $dd \rightarrow \alpha\gamma\gamma$ contribution to the background is shown by the blue curve in the top panel and the purple curve in the bottom panel [75]. In addition, another contribution due to $dd \rightarrow \alpha\pi^0\gamma$, shown by a blue curve, has been included in the bottom panel. See text for further details.

1. *Fitting Procedure*

Although we expect $dd \rightarrow \alpha\gamma\gamma$ to dominate the continuum in our measurements, there are two other allowed physical processes that can also contribute. One is $dd \rightarrow \alpha\pi^0\gamma$. The prompt γ here will have a maximum energy in the center of mass equal to the difference between the kinematic end point energy and the mass energy of the π^0 (1.5 MeV at the lower beam energy, and 3.0 MeV at the upper beam energy). This γ is undetectable by our apparatus. This process would yield a contribution to the missing mass continuum that extends from the π^0 mass to the kinematic end point.

The other physical process that could contribute is $dd \rightarrow \alpha\gamma\gamma\gamma$. This contribution is expected to be smaller than $dd \rightarrow \alpha\gamma\gamma$ by about a factor of 100, and is indistinguishable with our apparatus. We therefore did not consider it in our determination of the continuum.

In order to calculate the shape of the MM continuum arising from $dd \rightarrow \alpha\gamma\gamma$, we used cross sections for the process provided by Gardestig [75] to generate events in our computational model for the CSB apparatus. These events were processed just as the CSB events to create a MM distribution shape at each bombarding energy. In the final fitting only the normalization factor was allowed to vary.

In order to estimate the shape of the MM continuum arising from $dd \rightarrow \alpha\pi^0\gamma$, we assumed a pure kinematic phase space distribution of the three final state particles to generate events. These events were processed by our computational model of the CSB apparatus to generate the corresponding MM spectrum. We folded into this distribution a resolution width given by our fit to the CSB peak. In the final fitting, only its normalization factor was allowed to vary.

Parameters allowed to vary for the CSB Gaussian peak were its position, its width, and its height. In both fits the peak position had a fitting error of less than 60 keV and was consistent with the π^0 mass. At the lower energy the peak had a FWHM of 0.55 MeV, and at the higher energy a FWHM of 0.66 MeV. In each case, more than half the width was due to small changes in the offsets of the timing circuits over the period of data collection.

The results of the fitting are shown in Fig. 14. Evidence for the presence of $dd \rightarrow \alpha\pi^0\gamma$ is seen in the results at the higher energy, but none of significance was seen at the lower energy. This is consistent with an expected variation of this cross section as $k^3_{\gamma,max}$.

2. *CSB Yields*

Given the low statistics of the data, we decided to use the data itself as much as possible to obtain the CSB yields. The results of the fits were used to determine the regions over which we performed peak zone sums, and to obtain our estimates of the contribution of the continuum in that region.

At the lower beam energy (228.5 MeV), the peak zone consisted of 8 bins centered at 135 MeV/c^2. Each bin had a width of 0.2 MeV/c^2. The MM peak zone sum is obtained from the data. The MM continuum sum is obtained from the fit results in the peak zone region. The CSB events are obtained by taking the difference of the two sums. The results are shown in Table V. We obtain 73 ± 11 CSB events, which is 11% larger than

the yield reported in our earlier publication [12]. We estimate a systematic uncertainty of ±5 arising from our determination of the non-CSB continuum.

TABLE V. Factors and uncertainties for converting measured CSB yields into cross sections at 228.5 MeV and 231.8 MeV.

Quantity	228.5 MeV value	231.8 MeV value
MM peak zone width	0.8 MeV/c^2	1.0 MeV/c^2
MM peak zone sum	97 ± 10	86 ± 9
MM continuum sum	24 ± 5 (stat)	31 ± 6 (stat)
(in peak zone)	± 5 (sys)	± 6 (sys)
CSB peak events	73 ± 11 (stat)	55 ± 11 (stat)
	± 5 (sys)	± 6 (sys)
$\gamma\gamma$ det. eff.	0.3391 ± 0.0034	0.3206 ± 0.0032
channel acceptance	0.971 ± 0.001	0.794 ± 0.001
trigger efficiency	0.94 ± 0.01	0.96 ± 0.01
WC efficiency	0.93 ± 0.01	0.95 ± 0.01
system livetime	0.95 ± 0.01	0.94 ± 0.01
reaction losses	0.970 ± 0.005	0.970 ± 0.005
Lum. calib. acceptance	± 7.0%	± 7.0%
dp calib. cross section	± 5.0%	± 5.0%
$\int \mathcal{L}dt$ (pb^{-1})	19.2 ± 1.7	15.0 ± 1.3
Cross section (pb)	14.3 ± 2.2 (stat)	17.3 ± 3.4 (stat)
	± 1.6 (sys)	± 2.4 (sys)

At the higher beam energy (231.8 MeV), the peak zone consisted of 10 bins centered at 135 MeV/c^2. Each bin had a width of 0.2 MeV/c^2. The sums obtained are shown in Table V. Five of the events in the continuum sum in Table V come from the process $dd \to \alpha\pi^0\gamma$. We obtain 55 ± 11 CSB events, which is 10% larger than the yield reported in our earlier publication [12]. We estimate a systematic uncertainty of ±6 arising from our determination of the non-CSB continuum.

The final CSB yields reported here differ from those of the earlier publication [12] because the continuum under the CSB peak was treated differently. In the present work we modeled the underlying physical processes directly and used the computational model for the CSB apparatus to obtain the final MM spectrum. In our earlier work the underlying continuum made use of the large background of noncoincident alphas to approximate the channel transmittance at lower MM. These final results for the CSB yields have statistical uncertainties that still put them in agreement with the earlier reported results.

3. CSB cross sections and error budget

Listed in Table V are six correction factors needed to be applied to the CSB yields: the $\gamma\gamma$ detection efficiency, the channel acceptance, the trigger efficiency, the WC efficiency, the system livetime, and reaction losses. Included in the table are the values for the final integrated luminosities. Putting these quantities together one obtains the final cross sections for CSB, and the associated uncertainties, listed at the bottom of Table V. We find a cross section of 14.3±2.2 (stat) ± 1.6 (sys) at 228.5 MeV; and 17.3 ± 3.4 (stat) ± 2.4 (sys) at 231.8 MeV. These results are about 13% larger than those reported in the original publication [12].

This is the first time that both of these cross sections have been measured.

VI. DISCUSSION OF RESULTS

We present in this paper a discussion of a new evaluation of the results from a measurement of the $d + d \to {}^4\mathrm{He} + \pi^0$ reaction just above threshold. An extensive review was made of the features of the apparatus used in the measurement; new GEANT simulations were prepared; and a re-evaluation was completed of the $d + p$ elastic scattering data used as the reference reaction for the absolute cross section value. A better treatment of the background underneath the π^0 peaks as a function of missing mass has yielded a few additional events for the ${}^4\mathrm{He} + \pi^0$ reaction, thereby increasing the cross section. Some evidence has also appeared for the ${}^4\mathrm{He} + \pi^0 + \gamma$ channel on the high missing mass side of the peak at 231.8 MeV. Following our original publication [12], additional $d + p$ scattering data was published in this energy region with particular attention paid to the absolute normalization of the cross section [52]. This cross section is lower than the previous reference values, bringing our CSB cross sections back down, closer to their original publication values.

New measurements of the $dd \to \alpha\pi^0$ cross section angular distribution have been reported from COSY [76] at an excess energy of 60 MeV. These four new data points show a very strong $\cos^2\theta$ dependence, indicating that in addition to the S-wave part of the reaction there is a large D-wave component present at these energies. The S-wave is consistent with our near threshold measurements. Any P-wave piece that might be present appears to be small. Together, these measurements show a more detailed picture of this CSB reaction.

VII. CONCLUSIONS

This measurement of the $dd \to \alpha\pi^0$ total reaction cross section was undertaken with the realization that a credible result depended on a complete measurement of the final state. The Pb-glass array was chosen because the detectors are particularly insensitive to neutrons and charged particles while providing clear signals for energetic photons. The array was made to cover as much solid angle as possible so that the probability of capturing both photons was significant. We chose to operate in the Indiana electron-cooled storage ring since it offered precise tuning of the needed energy and the opportunity for a particularly thin windowless gas target. The choice

was made to use the 6° bend on the Cooler to capture the full cone of forward-going ^{4}He particles. The $pd \to h\pi^0$ reaction was chosen to calibrate the energy associated with the IUCF cooler ring circumference and the ring operating frequency. A long, refocusing magnetic channel was created to allow for the precise measurement of the ^{4}He recoil momentum. An electronic coincidence among all of the scintillator signals permitted a fast rejection of many unwanted backgrounds. It was possible to locate the CSB reaction signals within the background despite the low rate of about two per day since the efficiency was comfortably high for detecting prospect CSB events. In replay, it was possible to remove drifts in the time-of-flight data so that the reconstruction of the missing mass was good throughout the experiment.

This attention to these major issues of the measurement made it possible to find the relevant CSB events within the recorded data and to generate a clean representation of the two (and possibly three) photon events associated with recoil ^{4}He nuclei. This gave the first clear measurement of the total cross section for this important CSB reaction.

VIII. ACKNOWLEDGMENTS

We would like to thank all of the IUCF cyclotron staff who made this entire effort possible; especially V. Anferov, G.P.A. Berg, J. Doskow, D. Friesel, T. Hall, H.O. Meyer, R. E. Pollock, T. Rinckel, T. Sloan, K. Solberg, J. Vanderwerp and B. von Przewoski. We would also like to thank our hosts at the KVI who graciously allowed us to remeasure the d+p elastic scattering with polarized proton and deuteron beams using the BBS magnetic spectrometer system. This includes the entire cyclotron operations staff, N. Kalantar and his graduate students. We also want to express our special thanks to K. Sekiguchi from RCNP who was a full participant in these KVI measurements and who has been an important source of information about the RCNP measurements and polarization measurements in general over the past decade.

We acknowledge support from the US National Science Foundation grant PHY-1614545 and from the Indiana University Center for Spacetime Symmetries.

[1] S.A. Coon and R.C. Barrett, Phys. Rev. C **36**, 2189 (1987).
[2] J.A. Nolen and J.P. Schiffer, Ann. Rev. Nucl. Sci. **19**, 471 (1969).
[3] G.A. Miller, B.M.K. Nefkens, and I. Šlaus, Phys. Rep. **194**, 1 (1990).
[4] G.A. Miller and W.T.H. van Oers, in *Symmetries and Fundamental Interactions in Nuclei*, eds. W.C. Haxton and E.M. Henley (World Scientific, Singapore, 1995) p. 127; and references therein.
[5] Gerald A. Miller, Allena K. Opper, and Edward J. Stephenson, Ann. Rev. Nucl. Part. Sci. **56**, 253 (2006).
[6] U. van Kolck, Few Body Systems, Suppl. **9**, 444 (1995).
[7] U. van Kolck, J.A. Niskanen, and G.A. Miller, Phys. Lett. B **493**, 65 (2000).
[8] G. Miller and Bolton, Phys. Rev. D (2006).
[9] W.R. Gibbs, Li Ai, and W.B. Kaufmann, Phys. Rev. Lett. **74**, 3740 (1995).
[10] C. Matsinos, Phys. Rev. C **56**, 3014 (1997).
[11] A.K. Opper *et al.*, Phys. Rev. Lett. **91**, 212302 (2003).
[12] E.J. Stephenson *et al.*, Phys. Rev. Lett. **91**, 142302 (2003).
[13] A. Quenzer *et al.*, Phys. Lett. **76B**, 512 (1978).
[14] A. Filin, V. Baru, E. Epelbaum, j. Haidenbauer, C. Hanhart, A. Kudryavtsev, and U.-G. Meisner, Phys. Lett. B **681**, 423 (2009).
[15] W.N. Cottingham, Ann. Phys. **25**, 424 (1963).
[16] S.R. Beane, K. Orginos, and M. J. Savage, Nucl. Phys. B **768**, 38 (2007).
[17] A. Nogga, A.C. Fonseca, A. Garrdestig, C. Hanhart, C.J. Horowitz, G.A. Miller, J.A. Niskanen, and U. van Kolck, Phys. Lett. **B639**, 465 (2006).
[18] A. Gardestig, C.J. Horowitz, A. Nogga, A.C. Fonseca, C. Hanhart, G.A. Miller, J.A. Niskanen, and U. van Kolck, Phys. Rev. **C69**, 044606 (2004).
[19] J.A. Niskanen, Few Body Systems **26**, 214 (1999).
[20] K.R. Greider, Phys. Rev. **122**, 1919 (1961).
[21] A. Nogga, private communication (2016).
[22] A. Gardestig, D.R. Phillips, and Ch. Elster, Phys. Rev. C **73**, 024002 (2006).
[23] A. Gardestig *et al.*, Phys. Rev. C **69**, 044606 (2004).
[24] A.M. Micherdzinska *et al.*, Phys. Rev. C **75**, 054001 (2007).
[25] L.I. Lapidus, Zh. Eksp. Teor. Fiz. **31**, 865 (1956) [Sov. Phys. JETP **4**, 740 (1957)].
[26] J. Banaigs *et al.*, Phys. Rev. Lett. **58**, 1922 (1987); and references therein.
[27] L. Goldzahl, J. Banaigs, J. Berger, F.L. Fabbri, J. Hufner, and L. Satta, Nucl. Phys. **A533**, 675 (1991).
[28] D. Dobrokhotov, G. Faldt, A. Gardestig, and C. Wilkin, Phys. Rev. Lett. **83**, 5246 (1999).
[29] A. Gardestig, G. Faldt, and C. Wilkin, Phys. Rev. C **59**, 2608 (1999).
[30] G.A. Miller and E.J. Stephenson in the Research Proposal for IUCF Experiment CE78, "A Search for the Charge Symmetry Breaking Reaction $dd \to \alpha\pi^0$", May 30, 2000.
[31] This is now known as CEEM, the Center for Exploration of Energy and Matter.
[32] A.C. Betker *et al.*, Phys. Rev. Lett. **77**, 3510 (1996).
[33] Surface barrier silicon detectors manufactured by Perkin-Elmer Instruments, 801 S. Illinois Avenue, Oak Ridge, TN 37831.
[34] Photomultiplier tubes manufactured by Hamamatsu Corporation, 360 Foothill Road, Bridgewater, NJ 08807.
[35] L. Adiels *et al.*, Nucl. Instr. Meth. **A244**, 380 (1986).
[36] G. Xu *et al.*, Phys. Rev. C **52**, 2859 (1995).
[37] D. Hill *et al.*, Phys. Rev. Lett. **30**, 239 (1973).
[38] G. Burleson *et al.*, Phys. Rev. D **12**, 2557 (1975).
[39] D.L. Adams *et al.*, Phys. Lett. B **261**, 201 (1991).

[40] Infolytica Corporation, Montreal, Quebec, Canada.
[41] Kapton, a polyimide film produced by Du Pont Company, Wilmington, DE 19898.
[42] M.A. Pickar, A.D. Bacher, H.O. Meyer, R.E. Pollock, and G.T. Emery, Phys. Rev. C **46**, 397 (1992).
[43] V.N. Nikulin *et al.*, Phys. Rev. C **54**, 1732 (1996).
[44] K.L. Brown, D.C. Carey, Ch. Iselin and F. Rothacker: Transport, a Computer Program for Designing Charged Particle Beam Transport Systems. See yellow reports **CERN 73-16 (1973)** and **CERN 80-04 (1980)**.
[45] M. A. Pickar, H. J. Karwowski, J. D. Brown, J. R. Hall, M. Hugi, R. E. Pollock, V. R. Cupps, M. Fatyga, and A. D. Bacher, Phys. Rev. C **35**, 37 (1987).
[46] M. A. Pickar, private communication.
[47] S.N. Bunker, J.M. Cameron, R.F. Carlson, J. Reginald Richardson, P. James, W.T.H. van Oers, and J.W. Verba, Nucl. Phys. A **113**, 461 (1968).
[48] O. Chamberlain and M.O. Stern, Phys. Rev. **94**, 666 (1954).
[49] H. Postma and R. Wilson, Phys. Rev. **121**, 1229 (1961).
[50] K. Kuroda, A. Michalowicz, and M. Poulet, Nucl. Phys. **88**, 33 (1966).
[51] H. Shimizu, K. Imai, N. Tamura, K. Nishimura, K. Hatanaka, T. Saito, Y. Koike, and Y. Taniguchi, Nucl. Phys. **A382**, 242 (1982).
[52] K. Sekiguchi *et al.*, Phys. Rev. C **65**, 034003 (2002).
[53] K. Ermisch *et al.*, Phys. Rev. C **71**, 064004 (2005).
[54] N. Sakamoto *et al.*, Phys. Lett. B **367**, 60 (1996).
[55] R.E. Adelberger and C.N. Brown, Phys. Rev. **D**, 2139 (1975).
[56] H. Rohdjeß *et al.*, Phys. Rev. **57**, 2111 (1998).
[57] K. Sekiguchi *et al.*, Phys. Rev. Lett. **95**, 162301 (2005).
[58] Crystal Bailey, Ph.D. thesis, Indiana University, Bloomington, 2009.
[59] A. Ramazani-Moghaddam-Arani, Ph.D. thesis, University of Groningen, 2009.
[60] K. Hatanaka, private communication.
[61] K. Hatanaka *et al.*, Phys. Rev. C **66**, 044002 (2002).
[62] GEANT program library, http://wwwinfo.cern.ch/asdoc/geant.html3/geantall.html.
[63] L. G. Greeniaus, **TRIUMF Kinematics Handbook**, 2^{nd} Edition – September 1987.
[64] A. Auce *et al.*, Phys. Rev. C **53**, 2919 (1996).
[65] C. Bäumer *et al.*, Phys. Rev. C **63**, 037601 (2001).
[66] A. Korff *et al.*, Phys. Rev. C **70**, 067601 (2004).
[67] R. F. Carlson, Nucl. Instr. Meth. in Phys. Res. **A537**, 594 (2005).
[68] J. F. Lecollet *et al.*, Eur. Phys J **A5**, 321 (1999).
[69] J. R. Wu, C. C. Chang, and H. D. Holmgren, Phys. Rev. C **19**, 370 (1979).
[70] C. Bailey, private communication.
[71] A. Auce, R. F. Carlson, A. J. Cox, A. Ingemarsson, R. Johansson, P. U. Renberg, O. Sundberg, G. Tibell, and R. Zorro, Phys. Rev. C **50**, 871 (1994).
[72] G. Igo and B. D. Williams, Phys. Rev. **131**, 1251 (1963).
[73] F. E. Bertrand and R. W. Peelle, Phys. Rev. C **10**, 1028 (1974).
[74] J. R. Wu, C. C. Chang, and H. D. Holmgren, Phys. Rev. C **19**, 659 (1979).
[75] Gardestig, private communication 2010.
[76] P. Adlarson *et al.*, Phys. Lett. B **781C**, 645 (2018).